Experimental Study of the FEL with a Tapered Undulator and Numerical Simulations of Short Pulse Free Electron Lasers

Vom Fachbereich Physik
der Technischen Universität Darmstadt

zur Erlangung des Grades
eines Doktors der Naturwissenschaften
(Dr. rer. nat.)

genehmigte

D i s s e r t a t i o n

angefertigt von

Sergiy Khodyachykh
aus Kharkiv

Oktober 2002

Darmstadt
D 17

Referent:	Professor Dr. rer. nat. Dr. h.c. mult. A. Richter
Korreferent:	Professor Dr.-Ing. W. Seelig
Tag der Einreichung:	29.10.2002
Tag der Prüfung:	09.12.2002

Zusammenfassung

In der vorliegenden Arbeit wurde systematisch experimentell als auch theoretisch untersucht, in wieweit das "Tapern" des Undulators eines Freie Elektronen Lasers dessen Wirkungsgrad beeinflusst. Dazu sind die am supraleitenden Darmstädter Elektronenbeschleuniger S-DALINAC bei einer Elektronenenergie von 31 MeV und bei einer Wellenlänge von 7 μm durchgeführten Messungen analysiert worden. Der Tapering Effekt wurde für Werte von $\alpha = -16.48, -14.14, -9.44, -4.73, 4.74$ und 9.5 untersucht. Dabei zeigen die experimentellen Ergebnisse eine Erhöhung des FEL Wirkungsgrads von etwa 15% für Tapering Werte in der Nähe von $\alpha = -4.73$ und 4.74.

Die experimentellen Ergebnisse wurden mit den theoretischen Vorhersagen eines sehr aufwendigen Simulationsprogramms verglichen. Für diesen Zweck musste das Simulationsprogramm erheblich erweitert werden, um unter den Bedingungen des FEL am S-DALINAC einsatzfähig zu sein. Die Eingabeparameter des eindimensionalen Codes wurden, z.B. durch Vergleich mit der beobachteten zeitlichen Entwicklung des optischen Makropulses, an die experimentellen Gegebenheiten angepasst und für verschiedene Observable, wie z.B. die Kleinsignalverstärkung, die Leistungsänderungen als Funktion der Desynchronisation und die Linienbreite der Laserstrahlung, die aus am S-DALINAC und bei FELIX durchgeführten Untersuchungen mit einem ungetaperten Undulator resultieren, getestet.

Es zeigt sich, dass die mit diesem eindimensionalen Code erzielten Voraussagen in sehr guter Übereinstimmung mit den im Rahmen dieser Arbeit analysierten experimentellen Ergebnissen sowie mit den Messwerten vom TJNAF sind. Daraus wird ersichtlich, dass in der vorliegenden Dissertation erstmals der Einfluss des Taperings auf den Wirkungsgrad eines FEL-Oszillators nachgewiesen werden konnte und dass dieser Effekt auch durch die im Rahmen dieser Arbeit durchgeführten Simulationen vorhergesagt wird.

Summary

In the present work the influence of tapering with respect of the FEL efficiency has been systematically investigated for the Darmstadt FEL experimentally and theoretically. In this context the experiments performed at the electron accelerator S-DALINAC with an electron beam of 31 MeV at a wavelength of 7 μm were analyzed. The tapering was investigated for $\alpha = -16.48, -14.14, -9.44, -4.73, 4.74$ and 9.5. The experiment shows an efficiency increase of about 15% due to tapering in the vicinity of $\alpha = -4.73$ and 4.74.

The experimental data were compared with theoretical predictions based on an elaborate simulation program. This simulation program has been extended considerably in order to be applicable for the experimental conditions of the FEL at the S-DALINAC. The input parameters of the one dimensional code were adjusted to the experimental conditions *e.g.* the optical macropulse evolution and were tested for the observables for the untapered undulator with respect to the small signal gain, power desynchronization and line width obtained from measurements performed at the S-DALINAC and FELIX.

The predictions of this one dimensional code for the tapered case are in very good agreement with the present experimental data as well as with the results from the TJNAF. It can thus be stated that in the present thesis an effect of tapering with respect to the efficiency of the FEL was found for the first time for oscillator as predicted by the simulations carried out within the frame of the present work.

Table of Contents

1 Introduction

The main advantage of a Free Electron Laser (FEL) over conventional quantum generators is its ability to continuously tune the radiation frequency by changing the electron energy or parameters of the undulator. The radiation has a high coherence and almost diffraction divergence. The FEL is able to achieve a high level of output power. In conventional laser systems it is problematic to get such results because of thermal and non-linear effects in the active medium. Furthermore an FEL can provide hard X-ray radiation which is at present time unattainable by conventional quantum generators. Due to a narrow spectral width and a high spectral brightness FELs have also a big advantage over synchrotron radiation source. An FEL based on the multi-bunch storage ring principle can become a constituent part of a source of high-energy monochromatic polarized γ-quanta which are then used for the investigations in nuclear physics and the physics of elementary particles.

In 1971 J. M. J. Madey at Stanford University has laid the foundation of modern FEL theory [1] and in 1976 he and his group have successfully demonstrated the operation of the first FEL [2] at a wavelength of 3.5 μm. However, for the creation of highly effective lasers it was indispensable to have electron sources with low energy spread, high peak current and small emittance which appeared in early 80's in the form of linear accelerators at Stanford [3] and Los Alamos [4], respectively, and the storage ring in Orsay [5]. Successful lasing of these machines has lead to a mass development of FELs. In the early 90's already more than a dozen of FELs driven by rf linacs, storage rings, microtrons, inductive and electrostatic accelerators were in operation.

Today there are many types of FELs driven by different electron sources, equipped by undulators and optical resonators which allow to continuously change the parameters of the radiation as power, wavelength, spectral width, polarization *etc.* in a wide range. The mechanism of the interaction between the electron beam and the electromagnetic radiation is well understood and simple. The interaction conditions are well defined since the interaction takes place in vacuum. For this reason the FEL theory was successfully developed and was found to be in good agreement with the experiment. Its trustworthy predictions stimulated the development of numerous experiments. In the beginning, for the treatment

of an FEL a theoretical approach was realized in the framework of quantum mechanics and quantum electrodynamics. However, later on it turned out that the results obtained in the framework of classical electrodynamics were sufficiently precise. By solving Maxwell's equations in the one-particle current approximation it became possible to understand the dynamics of the electrons in the ponderomotive potential. With the increase of the current density, Coulomb forces and collective effects became important, but they can be well described by means of this theory. Despite the great success in the FEL technique, which is apparent in the construction of the large number of experimental and users facilities, there are still many problems demanding new original solutions for the increase of the efficiency and the improvement of spectral characteristics of the FEL.

In 1990 the superconducting Darmstadt electron linear accelerator (S-DALINAC) – one of the first superconducting linear electron accelerators in the world [6] went into operation. The accelerator was designed for experiments to study the electron-nuclear interaction. Already long before the first operation of the S-DALINAC the possibility to design a source of a continuous photon beam based on the S-DALINAC was investigated. The FEL project demanded the modification of some accelerator components: an intense electron gun, an injection of intense beam with a particular time structure into the superconductive accelerating structures, extraction of the beam after one acceleration into the undulator, dumping of the beam after passing through the undulator and the design and the development of the optical resonator and undulator itself. Difficulties connected with the low peak current, decrease of the longitudinal and transversal beam size and the choice of the optimal Reileigh length of the resonator have been overcome.

The FEL project was realized in 1996 with the following parameters [7]. The electron bunch has a time structure with a pulse length of about 2 ps spatially separated by the distance of approximately 30 m. The peak current reaches the value of 2.7 A. The homogenous hybrid wedged-pole undulator consists of 80 periods having the period length of 3.2 cm and a field strength between 0.15 and 0.4 T. An almost concentric resonator is formed by 2 multi-layered dielectric mirrors with a diameter of 5 cm, having a reflectivity up to 99.8% and are separated by a distance of 15.01 m. The FEL reaches saturation after approximately 2000 resonator round trips of the amplified light pulse. The Darmstadt FEL has macropulses with a typical length of 4 to 8 ms and is thus the source of cw light.

In the first experiments a beam with an average power of 3 W and a wavelength between 6.6 and 7.8 μm was obtained. The maximum small signal gain amounted to 3-5% and the *efficiency*, *i.e.* the ratio of the power of laser light to the electron beam power, to about 1.5%.

In general, the relatively low efficiency of the FEL is dissatisfying. Travelling down the undulator, the electron transfers part of its energy to the light wave and consequently leaves the resonant condition. That is why the efficiency of the FEL descends. Already at an early stage of the FEL development, undulators with a linear variation of the period length or of the field strength or both [3, 8] were proposed to reduce this effect. An undulator, modified in such a way was named *nonuniform* or *tapered* undulator contrary to the *uniform* one having both, a constant magnetic field and period. At the beginning, an efficiency increase by a factor of 2 to 3 was expected. Later, the free electron laser *amplifier* at Livermore using an undulator with a magnetic field decreasing along the undulator axis, a so-called *positively-tapered* undulator, has reached an efficiency increase [9] by a factor of 6. By means of numerical simulations it was predicted [10] that the efficiency of the FEL amplifier can be increased even further from 6% for the uniform case to 65% using a tapered undulator, *i.e.* over one order of magnitude.

The success of an efficiency increase in FEL *amplifiers* has stimulated theoretical and experimental interest in FEL *oscillators* using a tapered undulator. Saldin *et al.* showed [11, 12] that a mild *negative* tapering, *i.e.* with a magnetic field increasing along the undulator axis, should produce better extraction efficiency than a positive taper. Experiments conducted at two infra-red FEL facilities CLIO France [13] and FELIX Netherlands [14] yielded almost a doubling of the FEL efficiency using a two-section undulator with a negative step tapering [15,16]. Simultaneously it was observed that the small signal gain grows, that due to side-band suppression the spectral brightness of the FEL increases and that the laser operates more stable, generating smooth picosecond pulses. Recently, a further numerical simulation [17, 18] based on the parameters of the TJNAF FEL, also predicted that the use of a small negative tapering should result in an increase of the efficiency from 0.8% to 0.9% which should reflect itself in a saturated power increase of about 15%. However, experiments [19] conducted at the TJNAF FEL did not show any increase of the efficiency caused by tapering. On the contrary, the highest efficiency was observed for the uniform undulator. Along with the

efficiency enhancement, a noticeable decrease of the *small signal gain* has been theoretically predicted. This additionally complicates the study of the tapering phenomenon. For this reason it has been proposed [20] to apply *time-dependent* tapering. In this situation the magnetic field changes also in time and it has been predicted, that the FEL efficiency can be increased up to a value of 20%.

Thus, so far there is no experimental evidence for an efficiency increase with a linearly tapered undulator, in spite of the fact that there are many encouraging predictions. It has been the aim of the present work to investigate the influence of a tapered undulator on the main parameters of the Darmstadt FEL. In this context experimental data of spectral distributions taken at the Darmstadt FEL for different tapering values [21] had to be compared with predictions based on simulations for the interaction processes in the tapered undulator.

For this purpose the simulation code originally designed for the numerical study of an FEL amplifier [22] had to be extended to the conditions of the multi-pass Darmstadt FEL. An adjustment of the code input parameters had to be carried out and the code validity had to be proved by comparison to the results of other numerical simulations and measurements at FELIX and at the Darmstadt FEL with an uniform undulator. As soon as good agreement between predictions of the simulations with the results from the FELIX and the Darmstadt FEL with a uniform undulator has been achieved, a numerical study of the Darmstadt FEL working in the regime of a tapered undulator had to be carried out using the same input parameters of the simulation code.

The thesis is structured as follows. In Chapter 2 the basics of the theory of the FEL with the uniform undulator are introduced. The principles of tapering and the modifications which tapering introduces into the theory of the FEL with a uniform undulator are discussed in Chapter 3. Chapter 4 describes both experimental setups, the Darmstadt FEL as well as at FELIX which were used during the respective measurements. The numerical simulation code is introduced in Chapter 5, including a discussion of the limitations of the code. Chapter 6 summarizes the input parameters and the range of their tuning. The results of the simulation are compared with the experimental findings for a uniform undulator for several observables studied at the Darmstadt FEL and at FELIX (Chapter 7). Finally, the experimental results obtained with the tapered undulator of

the Darmstadt FEL are presented and compared with the numerical results in Chapter 9. The thesis closes with a summary and outlook.

2 Principle of the FEL

In this section the basic relations needed for the simulation of the observables are derived. After a short introduction describing the FEL principle in more general terms the following three sections deal with the influence of the electron beam quality on the electron motion inside the undulator, with the energy exchange between the electron beam and the optical field resulting in the bunching of the electron pulse distribution and with the changes of the optical wave amplitude caused by the bunching, respectively. The last three chapters treat the essential quantities that are of importance for the understanding of the present work *e.g.* the small signal gain, the saturation of the optical field and the inclusion of short pulse effects.

2.1 Introduction

Free electron lasers (FEL) generally differ from conventional laser systems. In conventional lasers electrons are bound and coherent radiation appears during their stimulated transition from an excited meta-stable level of an atom or molecule to the lower lying one. The radiation wavelength is given by the difference of the excitation energy of these levels and can not be tuned. The layout of an FEL is shown in Fig. 2.1. Passing through the alternating magnetic field of an undulator having N_u periods of the length λ_u, a relativistic electron beam experiences transversal oscillations. The electron trajectory can be calculated by solving the Lorentz equation without an electromagnetic wave and assuming *perfect injection*: electrons enter the undulator at the center of the gap with zero angle to the undulator axis. The transversal size of the real beam and its emittance lead to betatron oscillations and as a sequence to a dispersion of the phase velocity. This calls for a high quality of the electron beam: in order to keep the energy spread less than the amplification band the emittance should be less than π mm mrad.

The accelerated electrons radiate in forward direction. This radiation, called in analogy to the conventional laser *spontaneous emission*, is the "noise" from which

the optical generation *i.e.* the *lasing* starts. The experimental and theoretical study of the spontaneous emission is needed for a diagnostic tool of the beam transport and the undulator quality. The spectral width of the spontaneous emission line decreases with the number of the undulator periods.

This radiation is stored between two mirrors, which form an optical resonator. The resonator synchronizes the simultaneous circulation of the electromagnetic wave and the electron bunch and it focusses the radiation inside the undulator. Due to the transverse velocity of the electrons an energy exchange between electrons and the optical field takes place.

Solving Maxwell's equations assuming a slowly-varying field amplitude, the wave equation of the light amplified during the interaction with the beam current is obtained. The change in the amplitude of the electromagnetic wave, *i.e.* the *gain* is proportional to the average density of the electron-phase distribution and

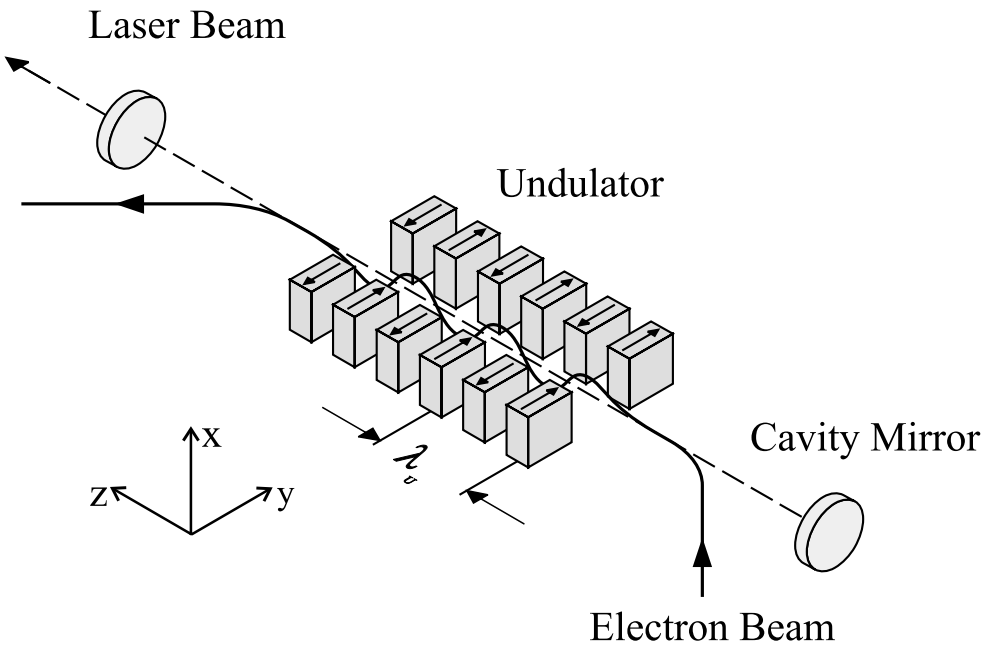

Fig. 2.1: Principle of an FEL. Relativistic electrons passing through the alternating magnetic field of the undulator with the period λ_u experience transversal oscillations and radiate spontaneously. This radiation is stored between two mirrors forming an optical resonator. The interaction between electrons and the optical field leads under certain conditions to the amplification of latter. Part of the optical power is extracted through one of the mirrors.

thus the bunching of the electrons is necessary condition of the amplification of the electromagnetic wave. Travelling inside the undulator together with the electromagnetic radiation the electrons interact with the latter. The ponderomotive potential of the electromagnetic wave leads to the beam bunching. As a result of this electrons are grouped by phase and start to radiate coherently, amplifying the electromagnetic wave. The wavelength of the radiation emitted by the electrons is defined by the spectral distribution of the *small signal gain* which is proportional to the derivative of the spectral distribution of spontaneous emission. The emitted wavelength can be tuned within a wide range by changing the strength of the undulator magnetic field or the electron energy.

During the lasing process electrons passing through the undulator can transfer part of their energy to the optical field, decelerate and shift from the amplification to the absorption part of the gain spectrum. To continue the energy transfer the electron needs an additional phase acceleration. It can be obtained by a smooth change of the undulator period or magnetic field along the undulator axis. Estimates show that the efficiency of FELs using an undulator modified in such a way can exceed the natural value of $\approx 1/2N_u$.

2.2 Electron dynamics inside the undulator

An electron bunch of a small transverse size and low angular divergence is injected exactly along the z axis into an idealized planar undulator having the magnetic field described by [23]

$$B\left(z\right) = \sqrt{2}B_y \sin\left(k_u z\right), \tag{2.1}$$

where $k_u = 2\pi/\lambda_u$ is the wave number of the undulator, λ_u and B_y are its period and rms field amplitude, respectively. The equation of the electron motion in the magnetic field is then given by

$$\gamma m \frac{d\vec{v}}{dt} = e\left(\vec{v} \times \vec{B}\right), \tag{2.2}$$

where $\vec{v}$ is the electron velocity, e and m are its charge and mass, respectively, c is the velocity of light, γ is the relativistic factor and $\left|\vec{B}\right| = B(z)$ is the magnetic

field strength directed along the y axis. In Eq. (2.2) spontaneous emission is neglected. The components of the equation of motion are given by

$$\frac{dv_x}{dt} = -\frac{\sqrt{2}v_z K c k_u}{\gamma}\sin(k_u z) \tag{2.3}$$

$$\frac{dv_y}{dt} = 0 \tag{2.4}$$

$$\frac{dv_z}{dt} = \frac{\sqrt{2}v_x K c k_u}{\gamma}\sin(k_u z), \tag{2.5}$$

with $K = eB_y/k_u mc$ being the *dimensionless undulator parameter*, which is usually close to 1. Taking into account that the transverse component of the velocity $v_x \ll v_z$ and $v_z \approx v_\parallel$, which is the electron velocity at the undulator entrance, integration of Eq. (2.3) with substitution of $k_u z = \omega_u t$ yields

$$v_x = \sqrt{2}\,(cK/\gamma)\cos(\omega_u t)\,. \tag{2.6}$$

Substituting v_x in (2.5) and integrating the latter one obtains

$$v_z = v_\parallel - \left(K^2 c^2/2\gamma^2 v_\parallel\right)\cos(2\omega_u t)\,. \tag{2.7}$$

The integration of the velocity components taking into account initial conditions, yields the coordinates of the electron trajectories at an arbitrary time point:

$$x = \sqrt{2}\,(Kc/\gamma\omega_u)\sin(\omega_u t) \tag{2.8}$$

$$y = 0 \tag{2.9}$$

$$z = v_z t - \left(K^2 c^2 k_u/4\gamma^2\omega_u^2\right)\sin(2\omega_u t) \tag{2.10}$$

Thus, the alternating magnetic field of a planar undulator results in electron oscillations along the x axis with the frequency ω_u. The longitudinal movement is a superposition of a forward movement and longitudinal oscillations with the doubled frequency - second term in (2.10). In the frame which moves with the longitudinal electron velocity its trajectory have a form of a figure "8". These oscillations cause spontaneous emission on the fundamental and on the harmonics. The relative power of harmonics grows [24] with K. In the case of the Darmstadt FEL their contribution can reach about 25 %.

From (2.6) and (2.7) the rms speed amplitude of transverse oscillations is

$$\overline{(v_x/v_z)} \approx \bar{\beta}_x = K/\gamma. \tag{2.11}$$

The maximum relative transverse velocity $\left(v_x/v_\parallel\right)_{\max} = \sqrt{2}\bar{\beta}_x$ corresponds to the maximum angle $\theta_{\max}$ on which the forwardly radiated photon will deviate from the undulator axis. The Darmstadt FEL has $\theta_{\max} = 0.026$ rad. Since this angle is considerably larger than that of diffraction divergence of the main mode of the resonator, $\Theta_0 = 9.35 \cdot 10^{-4}$ rad only the $\approx 1/N_u$ portion of the spontaneously radiated photons participate in excitation of the fundamental resonator mode.

In the real beam the electrons may be deflected transversally, e.g. along the y axis at the distance y_0 and injected at an angle θ_y with respect to the undulator axis. This leads to betatron oscillations, which elongate the electron path comparing to perfectly injected electrons and cause a decrease of its phase velocity ν to [24]

$$\Delta\nu_\beta \approx -\left[2\pi N_u/\left(1+K^2\right)\right]\left(K^2k_u^2y_0^2+\gamma^2\theta_y^2\right), \tag{2.12}$$

where N_u is the number of undulator periods. The electron beam quality is characterized by the emittance $\varepsilon_y = \bar{y}_0\bar{\theta}_y$. For this value the phase velocity dispersion $\Delta\nu_\beta \approx -2\pi N_u K k_u \varepsilon_y/\gamma$ should not exceed the amplification bandwidth $\sim \pi$. This limits the maximum emittance to $\varepsilon_y^{\max} \approx \gamma\lambda/2\pi N_u K$. For example, an emittance of $\varepsilon_y^{\max} \leq 0.8$ mm mrad is desirable for the Darmstadt FEL.

2.3 Electrons in an optical field

Energy exchange between an electron and co-propagating optical field is possible due to the transverse component of the electron velocity. In case of a helical undulator the vector of the electric field $\vec{E}$ and the transversal electron velocity $\vec{v}_\perp$ have the form [25]

$$\begin{aligned} \vec{E} &= E_0\left\{\vec{e}_x\cos\left[\omega\left(z/c-t\right)+\phi\right]+\vec{e}_y\sin\left[\omega\left(z/c-t\right)+\phi\right]\right\} \\ \vec{v}_\perp &= c\left(K/\gamma\right)\left[\vec{e}_x\cos\left(k_uz\right)-\vec{e}_y\sin\left(k_uz\right)\right], \end{aligned} \tag{2.13}$$

where E_0 is the amplitude of the electromagnetic field. If the field amplitude and the phase are slowly varying functions, then the energy lost or gained by the electron per unit of the undulator length has the form

$$\frac{dE_e}{dz} = -\frac{e}{v_z}\left(v_xE_x+v_yE_y\right) \approx -e\left(K/\gamma\right)\left\{E_0\cos\left[k_uz+\omega\left(z/c-t\right)+\phi\right]\right\}, \tag{2.14}$$

which can be expressed by

$$dE_e/dz = -e\,(K/\gamma)\,E_0 \cos\psi, \tag{2.15}$$

where the phase $\psi = k_u z + \omega\,(z/c - t) + \phi$ corresponds to the angle between the transverse velocity $\vec{v}_\perp$ and the vector of electric field $\vec{E}$. For an effective energy exchange between the electron and the optical field the scalar product $\vec{v}_\perp \cdot \vec{E}$ should be maximal and almost constant over the entire undulator length, *i.e.* the resonant condition $d\psi = k_u dz + \omega dz/c - \omega t = 0$ must be fulfilled. This condition can be rewritten in the form [25]

$$\frac{\lambda_u}{v_z} = \frac{\lambda}{c - v_z}. \tag{2.16}$$

The physical meaning of Eq. (2.16) is that synchronization between the electrons and the optical wave takes place when the wave advances the electron beam by one wavelength at one undulator period. Figure 2.2 illustrates the resonant condition. For relativistic electrons with $v_z \cong c$, the resonant condition can be rewritten in the form

$$\lambda_r \approx \lambda_u/2\gamma_z^2 = \lambda_u\big(1 + K^2\big)/2\gamma^2. \tag{2.17}$$

Electrons with different phases with respect to the optical wave get different energy increment. This results in a change of the longitudinal electron velocity v_z, combined with a change of energy E_e. Then the total derivative $d\psi/dz = k_u + \omega/c - \omega/v_z\,(E_e) \neq 0$. The violation of the resonance condition causes an electron phase change. If the particle energy E_e is close to the resonant energy E_e^r, the total derivative of the phase can be written [25] in the form

$$d\psi/dz = k_u + \omega/c - \omega/v_z\,(E_e) + \left[\omega/v_z^2\,(E_e^r)\right]\left[dv_z/dE_e\right](E_e - E_e^r). \tag{2.18}$$

The first three terms are constant over the entire undulator length and represent the phase velocity of the electron, $\nu = k_u + \omega/c - \omega/v_z\,(E_e)$. In case of the resonance, $E_e = E_e^r$, the phase velocity is equal to 0. Differentiating Eq. (2.18)

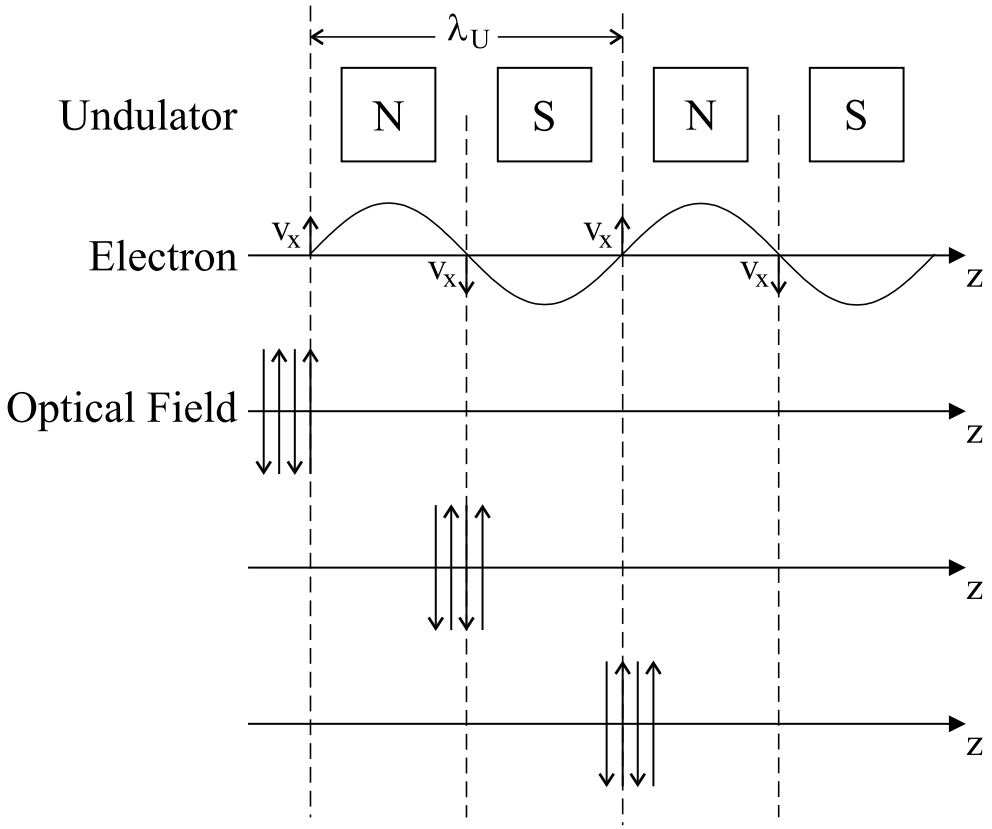

Fig. 2.2: Phase condition between the oscillating transverse component of the electron velocity of the electron and the optical field, which leads to the deceleration of the electron. The optical field, for which different phases are shown with arrows, has a higher velocity than the electron, so that a continuous phase shift takes place which is shown for three different values of time.

over z, the total derivative of the phase, once again and using the substitution (Eq. (2.15)) one obtains

$$d^2\psi/dz^2 + \left[e\omega\,(K/\gamma)\,E/\left(c\gamma_z^2 E_e^r\right)\right]\cos\psi = 0. \tag{2.19}$$

The phase ψ is the sum $\psi = \zeta + \phi$ of the electron phase related to the optical wave $\zeta = k_u z + \omega\,(z/c - t)$ and of the phase ϕ of the optical wave. Introducing [23] the new variables $\tau = z/L_u$ being *the dimensionless time* (so that $\tau = 0$ at the undulator enter and $\tau = 1$ at the undulator exit) and $u = 4\pi N_u e K L_u \bar{E}_0 e^{i\phi}/\gamma^2 mc^2$ being *the dimensionless optical wave amplitude* with $\bar{E}_0 = E_0/\sqrt{2}$, the equation

(2.19) may be simplified to the well-known pendulum equation

$$\ddot{\zeta} = |u| \cos(\zeta + \phi). \tag{2.20}$$

This equation is also valid for the planar undulator after the substitution $K \rightarrow K[J_0(\xi) - J_1(\xi)]$ in the dimensionless wave amplitude u. Here $\xi = K^2/2(1+K^2)$ with $J_0(\xi)$ and $J_1(\xi)$ being Bessel functions. The factor $[J_0(\xi) - J_1(\xi)]$ reflects the longitudinal oscillations of the electron in the planar undulator described by the second term in Eq. (2.10).

The phase velocity $\nu(\tau) = \dot{\zeta}(\tau)$ and the phase $\zeta(\tau)$ are the electron coordinates in the phase space. Electrons, entering the undulator ($\tau = 0$) are uniformly distributed over the phase. As it follows from the pendulum equation (2.20) for $\phi \approx 0$ the electrons with the phase $-\pi/2 \leq \zeta \leq \pi/2$ increase their phase velocity ($\ddot{\zeta} > 0$). For electrons with phase $\pi/2 \leq \zeta \leq 3\pi/2$ the phase velocity decreases, $\ddot{\zeta} < 0$. Thus the electrons tend to group around the phase $\zeta = \pi/2$. This process is called *bunching*. The dimensionless optical wave amplitude u characterizes the degree of the electron bunching. The pendulum equation is valid in both weak $u < \pi$ and strong $u \geq \pi$ optical fields.

2.4 Optical field inside the resonator

After a few round-trips the spontaneous emission stored inside the resonator has the form of classical plane wave. The electromagnetic radiation acts on the electrons which oscillate in the magnetic field of the undulator in a plane perpendicular to the undulator axis. The electrons interacting with the electromagnetic field in its turn also change the latter. To estimate the change of the phase and amplitude Maxwell's equation for the vector potential $\vec{A}(\vec{x}, t)$ is employed [23]

$$\left(\nabla^2 - \frac{1}{c^2}\frac{\partial^2}{\partial t^2}\right)\vec{A}(\vec{x}, t) = -\frac{4\pi}{c} J_\perp(\vec{x}, t), \tag{2.21}$$

where $J_\perp = -ec\vec{\beta}_\perp \delta^{(3)}(\vec{x} - \vec{r}_i)$ is the transversal component of the electron current, $\beta_\perp = -\left(\sqrt{2}K/\gamma\right)\cos(k_u z)$ and $\vec{r_i}$ is the electron radiusvector. In case of an idealized linear planar undulator the vector potential has the form

$\vec{A}(\vec{x},t) = (E_0(z,t)/k)\sin(\psi)$ with E_0 being the wave amplitude. Assuming that the amplitude and the phase of the optical wave are changing adiabatically, the second derivatives and the product of first derivatives in the left part of (2.21) are negligibly small. The slow change of the optical wave amplitude can be expressed by the inequalities $\dot{E}_0 \ll \omega E_0$ and $E_0' \ll kE_0$. The slow change of the optical phase reflects in the inequalities $\dot{\phi} \ll \omega\phi$ and $\phi' \ll k\phi$. Under these conditions (2.21) has the form

$$\left(\frac{\partial E_0}{\partial z} + \frac{1}{c}\frac{\partial E_0}{\partial t}\right)\cos\psi - E_0\left(\frac{\partial \phi}{\partial z} + \frac{1}{c}\frac{\partial \phi}{\partial t}\right)\sin\psi \approx \frac{-4\pi\sqrt{2}K}{\gamma}\cos(k_u z)\,\delta^{(3)}(\vec{x}-\vec{r}_i)\,. \tag{2.22}$$

Multiplying (2.22) by $\cos\psi$ and then by $\sin\psi$ and summing the result, the relation can be simplified. After averaging over the elementary length dL (which is much larger than the optical wavelength) with the constant time the left part of (2.22) has the form:

$$\left(\frac{\partial}{\partial z} + \frac{1}{c}\frac{\partial}{\partial t}\right)E_0 + iE_0\left(\frac{\partial}{\partial z} + \frac{1}{c}\frac{\partial}{\partial t}\right)\phi \tag{2.23}$$

The right hand side of (2.22) can be reduced to $\bar{\Phi} = \frac{1}{2}e^{-i\zeta}\left[J_0(\xi) - J_1(\xi)\right]e^{-i\phi}$ with the J_0 and J_1 being Bessel-functions. The substitutions $\xi = K^2/(2(1+K^2))$ and $\zeta = (k+k_u)z - \omega t$ are made here. Thus, (2.22) becomes

$$\left(\frac{\partial}{\partial z} + \frac{1}{c}\frac{\partial}{\partial t}\right)E_0 e^{i\phi} = -2\sqrt{2}\pi eK\left(J_0(\xi) - J_1(\xi)\right)\sum_i \frac{e^{-i\zeta}}{\gamma}\delta^{(3)}(\vec{x}-\vec{r}_i)\,. \tag{2.24}$$

The summation over all electrons is replaced by the average over the electron ensemble and weighted over the electron density n_e. For the electron bunch with uniform spatial distribution Maxwell's equation then has the form:

$$\left(\frac{\partial}{\partial z} + \frac{1}{c}\frac{\partial}{\partial t}\right)E_0 e^{i\phi} = -2\sqrt{2}\pi eK\left(J_0(\xi) - J_1(\xi)\right)n_e\langle\exp(-i\zeta)/\gamma\rangle \tag{2.25}$$

Inserting a new variable $z = \tilde{z} + ct$ (here $\tilde{z}$ is the coordinate which is related to the wave) the operator $\left(\frac{\partial}{\partial z} + \frac{1}{c}\frac{\partial}{\partial t}\right)$ reduces to $\frac{1}{c}\frac{\partial}{\partial t}$ and Eq. (2.25) has the form

$$\frac{1}{c}\frac{\partial}{\partial t}E_0 e^{i\phi} = -2\sqrt{2}\pi eK\left(J_0(\xi) - J_1(\xi)\right)n_e\langle\exp(-i\zeta)/\gamma\rangle. \tag{2.26}$$

Finally, after multiplication by the factor $4\pi N_u eK[J_0(\xi) - J_1(\xi)]L_u/\gamma^2 mc^2$ the relation (2.26) becomes

$$\dot{u} = -j\langle e^{-i\zeta}\rangle. \tag{2.27}$$

Here u is the dimensionless optical wave amplitude for the planar undulator defined in Sect. 2.3 and j is the dimensionless current density [23], defined as

$$j = \frac{8N_u \left(e\pi K \left(J_0\left(\xi\right) - J_1\left(\xi\right)\right) L_u\right)^2 n_e}{\gamma^3 mc^2}. \tag{2.28}$$

It follows from (2.27) that the optical wave amplitude u changes only if bunching takes place.

2.5 Small signal gain

The small signal gain is one of the most important parameters of an FEL with respect to the possibility of lasing. Despite the large success in FEL simulations, the analytical determination of the small signal gain makes it possible to understand the physics of the evolution of electron beams in the presence of an optical field, the origin and development of coherent radiation. At the same time the one-dimensional treatment is a sufficiently good approach [25]. Restricting the considerations to a low current density the intra-beam electron interaction can be neglected [26].

At the undulator entrance (dimensionless time τ=0) the electron coordinates in the phase-space are (see Sect. 2.3) the phase $\zeta_0 = \zeta\left(0\right)$ and the phase velocity $\nu_0 = \nu\left(0\right)$. In the low current density and weak optical field approximation the phase-space orbits of electrons are given [23] by $\nu\left(\zeta\right) = \pm\left(2H_0 + 2\left|u\right|\sin(\zeta+\phi)\right)^{1/2}$, where the constant of motion $2H_0 = \nu_0^2 - 2\left|u\right|\sin(\zeta_0+\phi)$ determines the individual path of the particle and is defined by initial conditions (ζ_0, ν_0). In the low gain limit there are stationary solutions, when neither phase nor phase velocity are changing in time. If electrons have initial positions in phase space $\nu_0 = 0$ and $\zeta_0 = \pi/2 \pm \pi p$, where $p = 1, 2, 3\ldots$, the vector of transverse velocity $\vec{\beta_\perp}$ and optical electric field $\vec{E}$ are orthogonal. Electrons do not exchange the energy with the optical field. Points $(\zeta_0 = 0, \nu_0 = \pi/2 \pm 2\pi p)$ are *stable fixed* points, and $(\zeta_0 = 0, \nu_0 = 3\pi/2 \pm 2\pi p)$ are *unstable*. Part of electrons with the space velocity $|\nu_0| \leq 2\sqrt{|u|}$ will be trapped into *closed*-orbits and those with the phase velocity $|\nu_0| \geq 2\sqrt{|u|}$ will travel on *opened* trajectories.

If an electron is not at a fixed point, then the interaction with the optical field changes its phase and amplitude. In the weak optical field the solution [23] of the pendulum equation (2.20) will be:

$$\zeta(\tau) = \zeta_0 + \nu_0\tau - \left(u_0/\nu_0^2\right)\left[\cos(\zeta_0 + \nu_0\tau) - \cos(\zeta_0) + \nu_0\tau\sin(\zeta_0)\right] + ... \quad (2.29)$$

$$\begin{aligned} \nu(\tau) &= \nu_0 + \left(\frac{u_0}{\nu_0}\right)\left[\sin(\zeta_0 + \nu_0\tau) - \sin(\zeta_0)\right] \\ &+ \left(\frac{u_0^2}{\nu_0^3}\right)\left[-(1/4)\left(\cos(2\zeta_0 + 2\nu_0\tau) - \cos(2\zeta_0)\right) + \cos(\nu_0\tau)\right. \\ &- \left. 1 - \nu_0\tau\sin(\zeta_0)\cos(\zeta_0 + \nu_0\tau)\right] + ... \end{aligned} \quad (2.30)$$

where the initial optical field is $|u(0)| = u_0$ and $\phi(0) = 0$. In a realistic electron beam electrons are distributed randomly over many (in case of the Darmstadt FEL about 85) optical wavelengths. Using only the first-order terms of (2.30) one can get the phase-distribution function of electrons inside the undulator:

$$f(\zeta,\tau) = \left(\frac{n_e}{2\pi}\right)\left(1 + \left(\frac{u_0}{\nu_0^2}\right)\left[\sin(\zeta - \nu_0\tau) - \sin(\zeta) + \nu_0\tau\cos(\zeta - \nu_0\tau)\right]\right) + ... \quad (2.31)$$

At the initial moment of time $\tau = 0$ the electron distribution is uniform. With the increase of τ the density modulation develops. While passing the undulator the electrons form groups around the phase $\zeta = \pi/2 \pm \pi p$, where $p = 1, 2, 3\ldots$ This process is called *bunching*. The rate of bunching is defined by the optical field strength u_0. Part of electrons with the $|\nu_0| \leq 2|u|^{1/2}$ is trapped onto closed orbits, bunches and radiate coherently.

Bunching of electrons is the basic reason of the gain mechanism. Starting at the resonance with $\nu_0 \approx 0$ the electrons start to bunch near the phase $\zeta \approx \pi/2$. The phase of the optical wave changes while the amplitude remains constant. Electrons entering the undulator with the phase velocity $\nu_0 \approx \pi$ drift, overpopulating the phase $\zeta \approx \pi$ and the amplitude of the optical field increases. Contrary to that electrons with $\nu_0 \approx -\pi$ overpopulate the phase $\zeta \approx 0$ and the optical field amplitude decreases, the FEL starts to absorb. The change of the optical field caused by these processes is characterized by the *small signal gain*.

The small signal gain is defined as

$$g = \frac{(\bar{E}_{in} + \Delta E)^2}{\bar{E}_{in}^2} - 1 \approx \frac{2\Delta E}{\bar{E}_{in}}, \quad (2.32)$$

where $\bar{E}_{in}$ is the optical field amplitude at the undulator enter and ΔE is the increase of the amplitude per one undulator pass. This equation can be expressed [23] in terms of phase velocity and time:

$$g = j\,(2 - 2\cos\nu_0\tau - \nu_0\tau\sin\nu_0\tau)/\nu_0^3 \tag{2.33}$$

The behavior of the function (2.33) is shown in Fig. 2.3. The function $g(\nu_0)$ is antisymmetric with respect to $\nu_0 = 0$ (see Fig. 2.3, top). The gain function reaches its maximum at the value $\nu_0 = 2.6$. The width of the amplification band $\Delta\nu_0 \approx \pi$. The change of the phase velocity at $\Delta\nu_0 \approx 2\pi$ changes the FEL interaction from amplification to absorption. This limits the energy spread of the electron beam.

The Darmstadt FEL has fields $u > \pi$. The wave equation and pendulum equation are also valid in strong optical fields ($|u| > \pi$). Strong optical fields lead to a trapping of the large part of electrons on the closed orbits and their bunching. The distribution function $f(\xi)$ becomes more complicated compared to the sinusoidal function (2.31). Optimal bunching is achieved already in part of the undulator. In strong optical fields the gain spectrum $g(\nu_0)$ changes its form. With the growth of initial field u_0, the maximum of the gain spectrum decreases, the position of the maximum shifts towards higher ν_0 and the gain curve becomes brighter.

2.6 Saturation

In strong optical fields electrons shift from the amplification band to the absorption region already in part of the undulator length. The absorption of the optical wave energy by electrons increases. In order to follow the onset of saturation the wave equation (2.27) should be rewritten [27] in the form

$$u(\tau) = u_0 + u_0 j\chi_1(\nu_0\tau) - u_0^2 j\chi_2(\nu_0\tau) + \ldots, \tag{2.34}$$

where $\chi_1(\nu_0\tau)$ and $\chi_2(\nu_0\tau)$ are complex functions with magnitudes of order unity. The real part of the function (2.34) is the small signal gain g while the imaginary part represents the phase shift of the optical wave. With the growth of the optical wave amplitude u the third term causes the decrease of the amplitude growth.

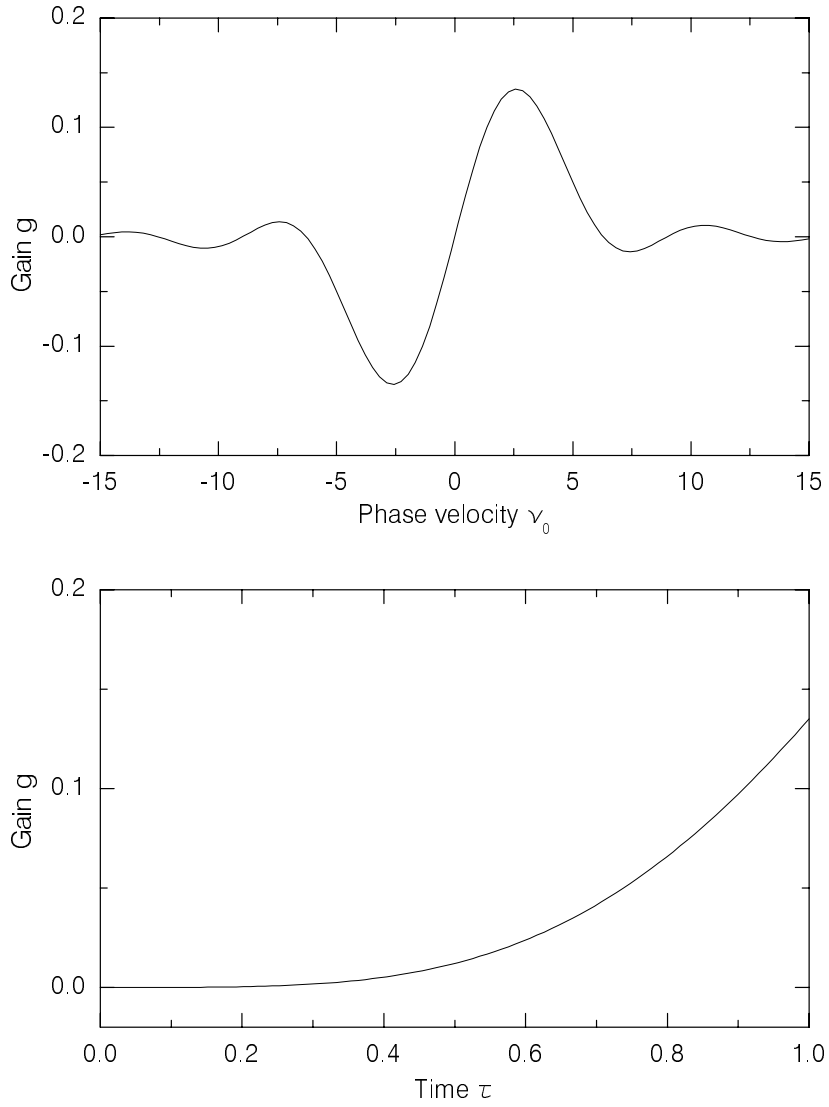

Fig. 2.3: Gain as a function of the phase velocity (top) and of the dimensionless time $\tau = ct/L_u$(bottom) calculated using (2.33) for the dimensionless current density $j = 1$. The small signal gain vs. phase velocity calculated at the exit of the undulator at $\tau = 1$, is antisymmetric with respect to ν_0 and has the maximum at the value $\nu_0 = 2.6$. For this value of ν_0 the gain evolution inside the undulator is shown (bottom) as the electrons travel from the undulator entrance ($\tau = 0$) to the undulator exit ($\tau = 1$).

The change in the field amplitude as a function of the number of passes through the undulator n is described by the expression

$$du/dn = j\,|\chi_1(\nu_0)|\,u_n - j\,|\chi_2(\nu_0)|\,u_n^2. \tag{2.35}$$

At the beginning of the oscillator operation when the optical field is still weak, the second term does not contribute much and the field grows exponentially. With the growth of the field amplitude the contribution of the second term becomes significant. This is the beginning of the saturation.

Also, resonator losses have to be taken into consideration and then (2.35) transforms into

$$du/dn = (j\,|\chi_1(\nu_0)| - \hat{\sigma})u_n - j\,|\chi_2(\nu_0)|\,u_n^2, \tag{2.36}$$

with $\hat{\sigma}$ being the dimensionless loss parameter.

The equality $du/dn = 0$ means the steady regime which corresponds to the FEL saturation. At saturation the field amplitude and efficiency is defined by the dimensionless loss parameter $\hat{\sigma}$. For a *cold* electron beam, *i.e.* without energy spread, the efficiency reaches its maximum value $\hat{\eta} = 3.6/4\pi N$ at $\hat{\sigma} = 0.028$. In the real electron beam the maximum efficiency is always lower because of the energy spread and shifts towards lower $\hat{\sigma}$.

2.7 Short pulse effects

For the successful operation of the FEL the electron beam should satisfy the following requirements. First, for the infrared or visual spectral regions the typical undulator period of few cm and undulator K-value of about one unit require a relativistic electron beam energy. At the same time, since the FEL gain is proportional to the beam current density (2.33), a high beam current density is required. And finally, the energy spread should be small compared to the width of the gain curve (see Sect. 2.5).

Based on the above specified criteria, most FEL facilities operating in the infrared region use radio-frequency (rf) linear accelerators. This type of accelerators

produce a train of short *ps* pulses. The light wave inside the resonator shows also this structure and thus consists also of a train of short micro pulses.

During the FEL interaction, electrons slip back relative to the optical pulse for two reasons: (i) the electron velocity is always smaller than the velocity of light and (ii) the electrons travel along the oscillating trajectories inside the undulator. The resonance condition (Sect. 2.3) requires that the electron bunch slips back by one optical wavelength λ per one undulator period. At the exit of the undulator consisting of N_u periods, the electron has slipped back by a *slippage distance* of $N_u\lambda$. If this quantity is comparable to the electron bunch length σ_z, short pulse effects should be taken into account.

In the small signal regime the emission grows toward the downstream end of the undulator where the electrons have shifted back relative to the front of the optical macropulse, the optical pulse peaks up at its rear. This has the consequence that the effective optical group velocity is somewhat smaller than its vacuum value. In a perfectly synchronized resonator the micro pulse will continue to narrow during the subsequent round trips. The reduced overlap between electron bunch and optical pulse will in turn reduce the gain. This effect is known as *"laser lethargy"*. In order to restore the gain it is necessary to slightly reduce the cavity length from the value giving the perfect synchronization. For convenience the cavity-length change is expressed usually in units of the optical wavelength $\Delta L/\lambda$.

On the other hand there is the problem that it is impossible to maintain the synchronism during both the growth phase and the saturated phase with a fixed cavity length. This is due to the fact that the optical group velocity returns to the vacuum value as the gain decreases and the power saturates. The loss of the synchronism has the consequence that a new pulse develops from the tail of the initial pulse.

In FELs operating with electron bunches longer than the slippage distance $N_u\lambda$ it has been observed that at saturation the initially smooth laser pulse breaks up into a train of short spikes [28] separated by the slippage distance [29]. This can be explained by the fact that at high optical power the electrons are bunched at the earlier stage of the undulator, but can later on reabsorb a part of the stored energy. In combination with slippage this leads to a longitudinal modulation of the optical field intensity.

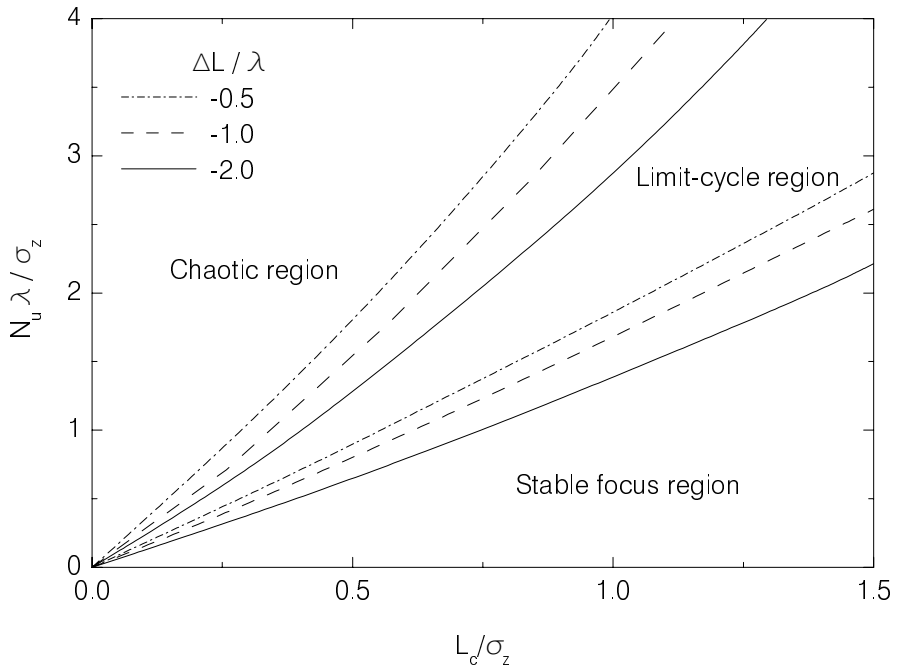

Fig. 2.4: Phase diagram [29] for different regimes of operation of an FEL oscillator. The quantities $N_u\lambda$ and σ_z are the slippage distance and the electron bunch length, respectively, and $L_c = \lambda/4\pi j$. Lines corresponding to three different cavity desynchronizations separate three different regimes of operation namely stable focus, limit-cycle and chaotic regimes.

For FELs with electron bunches shorter than the slippage distance it was shown theoretically [30] that spikes are not separated by the slippage distance but by the synchrotron length. The *synchrotron length* L_{syn} is the slippage of the electron over one full synchrotron oscillation of the electron in the ponderomotive potential. If the electron bunch is even shorter than the synchrotron length only the single spike can grow within the electron bunch. At saturation this spike moves forward with each successive round trip and finally loses the contact with the active medium. Because of the round-trip loss this pulse decays, while a new one is generated behind the first one. The process is then repeated with this new pulse. The formation of a train of subpulses leads to a stable limit-cycle oscillation of the macropulse power.

Hahn and Lee [29, 30] have shown that the various regimes of FEL operation can be identified for the set of parameters $\Delta L/\lambda$, $N_u\lambda/\sigma_z$ and L_c/σ_z. The last parameter contains the cooperation length $L_c = \lambda/4\pi j$ which is equal to the

slippage in one gain length. The phase diagram [29] for different regimes of the FEL operation is shown in Fig. 2.4. For the constant L_c/σ_z with the growth of $N_u\lambda/\sigma_z$ regimes change from the stable focus (when no subpulses develop) to the limit cycle region with sidebands in the spectrum. These sidebands double sequently (period-doubling). And finally the chaotic regime starts. In this regime each macropulse evolves in its own way which can also be observed in the spectral distribution. To reach the limit-cycle and chaotic regime, L_{syn} should become smaller than $N_u\lambda$. This means that the intracavity power has to saturate at a sufficiently higher level.

In Sect. 7.2 an experimental observation of the limit-cycle behavior at FELIX is introduced.

3 Tapering

3.1 Introduction

When the FEL reaches saturation, electrons lose energy and move from the amplification band to the absorption band on the gain curve (see Fig. 2.3). To keep the resonance between the electrons which loose the energy and the wave, an additional phase acceleration which is the function of the electron position inside the undulator should be imparted. This additional acceleration can be accomplished by a continuous decrease of the undulator period or a decrease of the magnetic field strength (Fig. 3.1, middle) or both [23, 31]. It was also predicted theoretically that for certain conditions an inverse tapering (Fig. 3.1, bottom) is more preferable. It is expected that in these cases electrons will continue to transfer their energy to the optical field in the undulator if their phase deceleration is compensated by the artificial acceleration. The tapering of the undulator in case of an FEL amplifier has shown almost 600% increase of the radiation intensity [9].

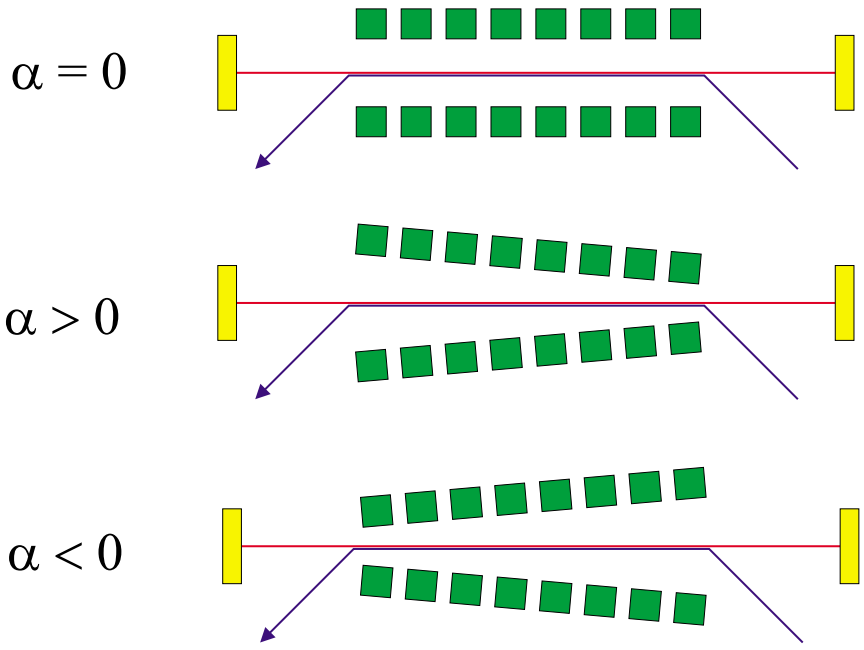

Fig. 3.1: Schematic principle of a uniform undulator (top), positive tapering (middle) and negative tapering (bottom). The drawing is not to scale. The real change of the undulator gap amounts to few per cent only.

In case of an FEL oscillator the problem is more complicated [12] and is solved less successfully.

In the following sections the basics of the tapering mechanism will be explained for the positive (Sect. 3.2) and negative (Sect. 3.3) tapering using the phase-space displacement method [32]. And in Sect. 3.4 the influence of tapering on the lasing wavelength, on the spectral distribution of the small signal gain and on the efficiency of the laser light output will be discussed.

3.2 Positive tapering

In the uniform undulator saturation sets in when the interaction with the optical field decelerates the electrons below the resonance. Further interaction with the electromagnetic wave increases the electron phase so that electrons start to absorb the energy of the electromagnetic wave and reduce the gain and efficiency. One way to avoid this is to redesign the downstream edge of the undulator to lower the resonant energy to a value below the resonant energy of the decelerated electrons (Fig. 3.1, middle).

Figure 3.2 shows three snapshots of the phase space at (1) undulator entrance, (2) undulator center and (3) undulator exit. The initial electron distribution is drawn as a rectangle, illustrating the uniform distribution of electrons in phase (horizontal direction) and electron energy spread (vertical direction) around $\nu_r(0)$. Electrons captured inside the bucket at the beginning of the undulator remain trapped inside the bucket throughout the undulator, provided that the undulator magnetic field varies adiabatically. The change in the magnetic field strength reflects itself in the decrease of the resonant wavelength so that the bucket is descending in phase space. The electrons in the bucket decelerate with the bucket and lose an essential part of their energy, more than it would be possible from motion inside a stationary bucket.

3.3 Negative tapering

The negatively-tapered undulator (Fig. 3.1, bottom) looks just opposite to the positively tapered undulator, described in section 3.2. The method of additional energy extraction in an FEL with a negatively tapered undulator principally differs from that of the positively-tapered case. Contrary to the positively tapered undulator, in this case the empty bucket is accelerated and moves upward in phase space as shown in Fig. 3.3. Since, according to Liouville's theorem phase space is conserved, when the bucket moves upward and the rest of phase space moves downward. The electrons are displaced downward in phase space and, thus are losing their energy, amplifying the optical field.

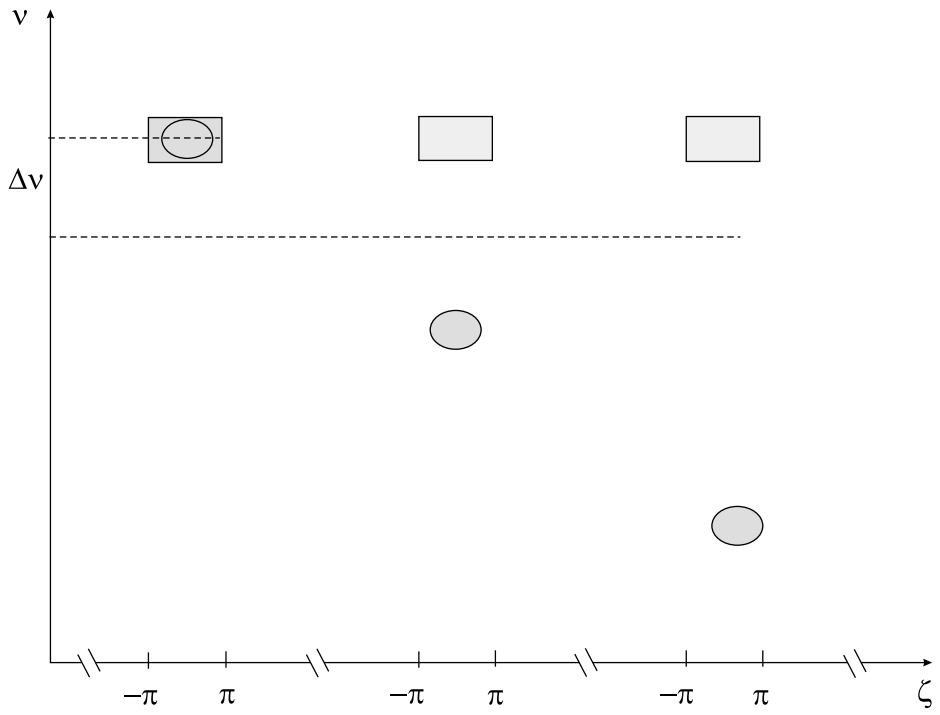

Fig. 3.2: Three snapshots of buckets for positive tapering at the undulator entrance (1), the undulator center(2) and the undulator exit(3). The initial electron distribution is shown in form of a rectangle, illustrating the uniform distribution of electrons in phase (horizontal direction) and energy spread (vertical direction). Electrons trapped in the bucket at the undulator entrance remain trapped throughout the undulator, thus losing an essential part of their energy.

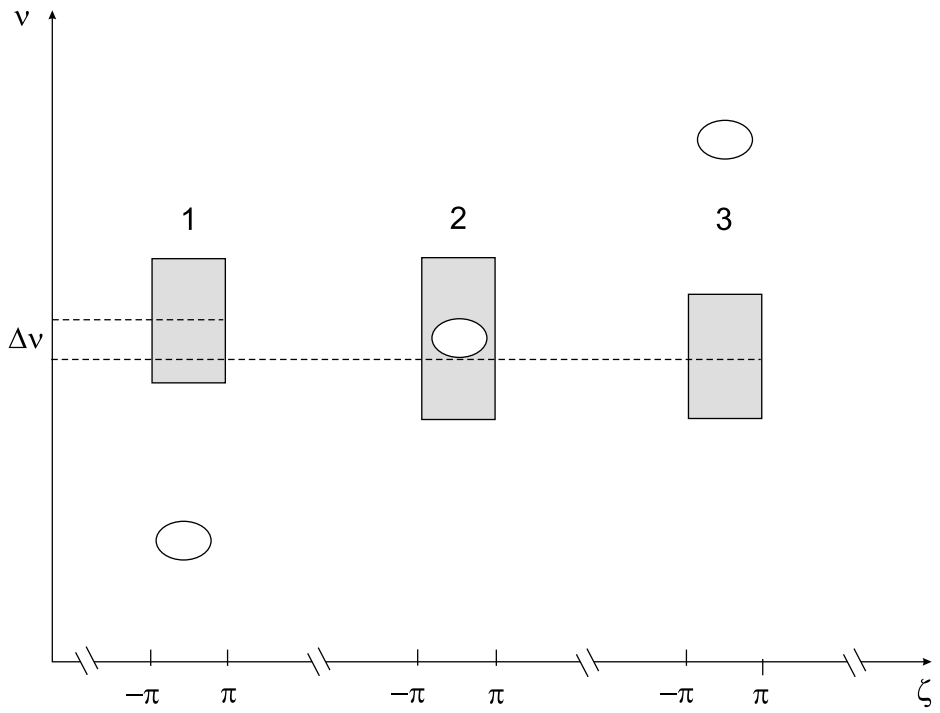

Fig. 3.3: Three snapshots of buckets due to negative tapering at the undulator entrance (1), the undulator center(2) and the undulator exit(3). The empty bucket is accelerated and moves upward in phase space. The phase space is conserved according to Liouville's theorem, the bucket moves upward and the rest of phase space moves downward, decreasing the average electron phase velocity on the value $\Delta\nu$.

3.4 Influence of tapering on the main FEL parameters

Tapering of the undulator magnetic field influences the FEL performance which can be understood analytically by solving the slightly modified pendulum (2.20) and wave (2.27) equations. For tapered case they have the form [23]:

$$\ddot{\zeta} = \alpha + |u| \cos(\zeta + \phi), \quad \dot{u} = -j\langle e^{-i\zeta} \rangle, \tag{3.1}$$

where $\zeta = \int_0^\tau k_u(\tau')\, d\tau' + kz - \omega t$ and $\alpha \approx -2\pi N_u K^2 \Delta B_u / [B_u(1 + K^2/2)]$. The quantity α is called the *tapering depth* or *tapering parameter*. Equations (3.1) are valid in weak and strong fields with high and low gain but only for low efficiency

($\leq 10\%$). According to these relations, electrons starting around the phase $\zeta \approx 0$ in phase space are accelerated by both the tapering α and by the optical field u. They move away from the absorption region and thus stop the interaction with the electromagnetic field. For the electrons which start near the radiation phase $\zeta \approx \pi$ the tapering α and the field u are subtracted and the electrons remain trapped on the closed orbits in the region of the gain maximum. Electrons, accelerated from the absorption maximum finally deposit less energy into the interaction. That is why it is expected that tapering leads to the increase of the efficiency.

In the tapered undulator the instantaneous trajectories in the phase-space are changed compared to the uniform trajectories (2.29, 2.30) by an additional pendulum rotation α as described by the second term on the right hand side according to [23]

$$\nu(\zeta) = \left[S_0 + 2\zeta\alpha + 2|u|\sin(\zeta + \phi)\right]^{1/2}, \tag{3.2}$$

where the initial conditions are defined by the value $S_0 = \nu_0^2 - 2\zeta_0\alpha - 2|u|\sin(\zeta_0 + \phi)$. The separatrix, which separates closed and open orbits, is defined in the case when $\phi = 0$ by $\nu_s^2 = 2\alpha(\zeta_s - \zeta_0) + 2|u|(\sin\zeta_s - \sin\zeta_0)$ where $\zeta_0 = 2\pi - \cos^{-1}(\alpha/|u|)$. In weak fields the small signal gain spectrum of the FEL with the tapered undulator is no longer antisymmetric with respect to zero [23].

Figure 3.4 shows the small signal gain profiles for two different positive values of the tapering parameter α. For comparison the small signal gain profile for the uniform undulator (see Fig. 2.3, top) is shown. The curves were obtained using the program package FEL1D [33] assuming an infinitely long monoenergetic electron beam. It is clearly seen that the curves are antisymmetric with respect to the point $\nu_0 = -\alpha/2$. The value of g at the first maximum dominates at $\alpha = 0$ (see Fig.2.3, top) and is decreasing rapidly with the growth of parameter α. It was found [11] that at $\alpha \simeq 26$ the first maximum becomes less that the second one. Further, the second maximum dominates till $\alpha \simeq 38$, etc. All experimental results which are analyzed in Chap. 9 were obtained in the region where the first maximum dominates. The gain in the maximum is less than in an uniform undulator regardless of the tapering sign. In weak fields the width of the gain spectrum is still $\Delta\nu \approx \pi$.

A more exact position of the first maximum [11] is described by $\nu_0^{\max} = 2.6 - \alpha/2 - y_1(|\alpha|)$ and of the second maximum by $\nu_0^{\max} = 10.6 - \alpha/2 - y_2(|\alpha|)$, where y_1

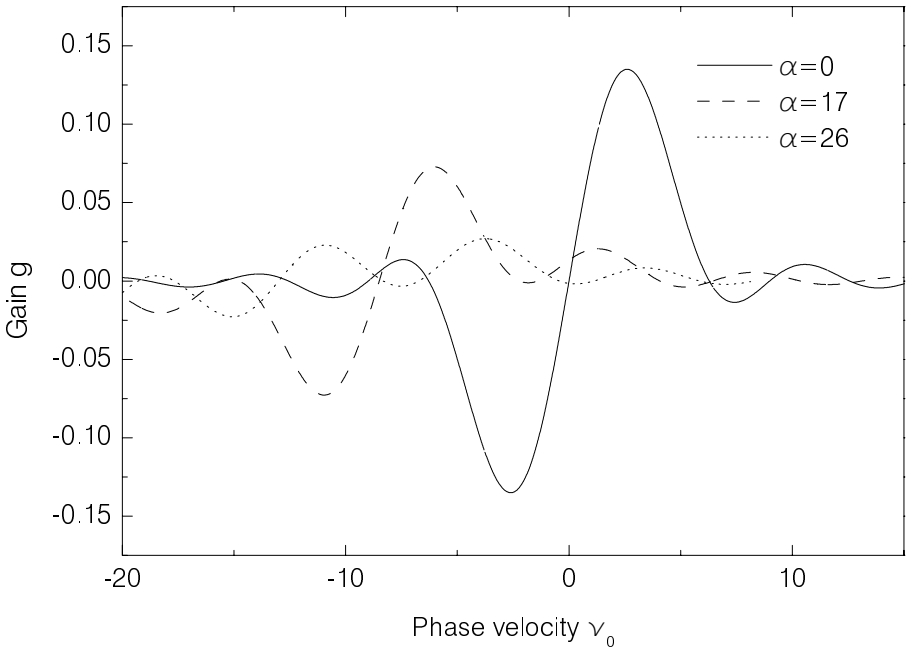

Fig. 3.4: Gain profiles for different values of the tapering depth α. Each curve is antisymmetric with respect to the initial phase velocity values ν_0 =0, -8.5, -13 for $\alpha = 0$ (solid line), 17 (dashed line) and 26 (dotted line), respectively. The value of the small signal gain g at the first maximum, dominating for $\alpha = 0$ and 17, decreases rapidly with the growth of α and becomes less than the value g at the second maximum for α =26.

and y_2 are positively valued functions of the absolute value of α. These functions give the small contribution to the change of $\nu_0^{\max}$ so that $y_{1,2} \ll |\alpha|$. Such a complicated behavior of the lasing wavelength results in nontrivial consequences for the efficiency optimization. In strong optical fields the gain spectrum changes but differently for positive and negative tapering [11, 34].

Not only the position of the radiation maximum but also the efficiency of the laser light output changes in the tapered undulator. The behavior [25] of the reduced efficiency $\hat{\eta} = 4\pi N_u \eta$ as a function of the tapering depth α is shown in Fig. 3.5 for both, positive (solid line) and negative (dashed line) values of the tapering depth α. It is predicted that up to the tapering depth of $|\alpha| \approx 12$ the efficiency of the laser light output is almost equal for both, negative and positive tapering depths. In this region an increase of the efficiency by a factor of up to 1.8 is predicted. A further increase of the tapering depth results in a decrease of the efficiency for

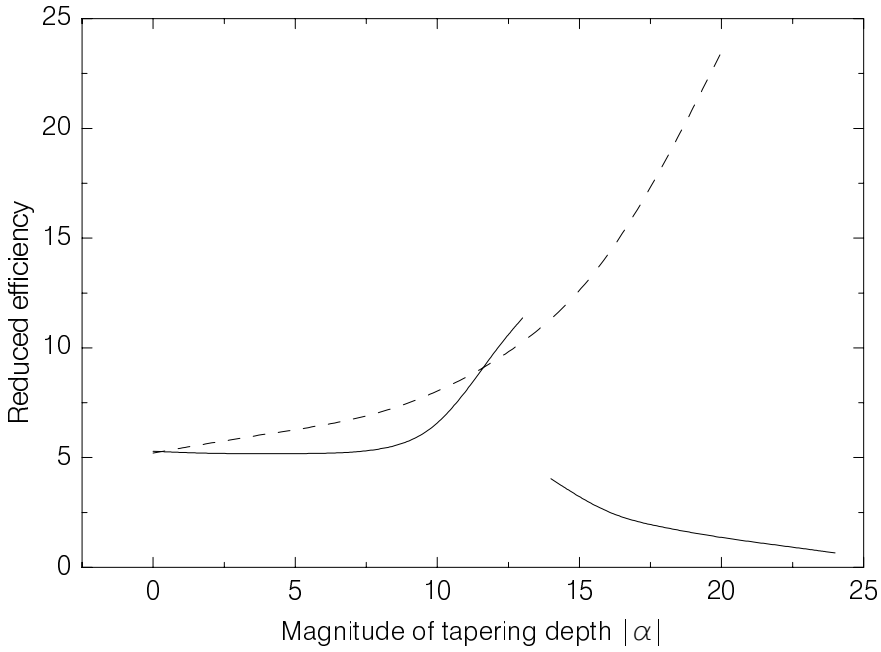

Fig. 3.5: The reduced efficiency $\hat{\eta} = 4\pi N_u \eta$ of the laser light output of the FEL oscillator as a function of the magnitude of the tapering depth $|\alpha|$. The solid line corresponds to the positive ($\alpha > 0$) and the dashed line to the negative values of α. The curves are obtained neglecting short pulse effects [25] for the undulator with $N_u = 80$ periods.

the positive tapering. In case of negative tapering an increase of the efficiency of the laser light output by almost a factor of 3.5 is predicted.

It thus can be stated, that the problem of the FEL efficiency increase in a one-section tapered undulator is not simple with respect to the theoretical investigation, since the lasing frequency is a function of the tapering depth and is defined by the maximum gain in linear regime of operation.

4 Experiments

4.1 S–DALINAC and the FEL

The superconducting electron linear accelerator S–DALINAC is in operation at the Institute of Nuclear Physics of the Darmstadt University of Technology since 1991. It is used for experiments on nuclear and radiation physics and since 1996 also as a driver for the infra red FEL [36]. Using the high-frequency accelerating method and dual beam recirculation, a continuous beam with the energies between 2.5 and 120 MeV can be produced [6].

Figure 4.1 shows the layout of the S–DALINAC and related experiments. The thermionic gun emits electrons, which are preaccelerated in an electrostatic accelerating section up to the kinetic energy of 250 keV. A chopper-prebuncher section, which consists of a normal-conducting high-frequency resonator prepares the beam necessary for the following high-frequency accelerating at a time structure of 3 GHz. At the injector entrance the electron bunches arrive with a length of 5 ps separated by 333 ps with an average current up to 60 μA. The injector consists of a 2-cell capture section as well as of one 5-cell and two 20-cell structures with the operational frequency of 3 GHz. These superconducting structures are manufactured of Niobium and are cooled down [37] to the temperature of 2 K. The injector accelerates the beam up to an energy of 10 MeV. Straightforward behind the injector the beam can enter the experimental area [38] for (γ, γ')-experiments [39], (γ, n)-experiments [40] as well as for experiments dealing with low-energy channelling and parametric X- radiation [41, 42]. Alternatively it can be injected by a 180° bending magnetic system into the superconductive main accelerator. It consists of eight 20-cell cavities and enables an energy increase up to 40 MeV. To increase the energy further the beam can be recirculated once or twice. Thus, electrons have a maximum energy of 130 MeV at the exit of the accelerator. They are used in the experimental hall for electron-scattering experiments in two high-resolution spectrometers, for experiments in radiation physics in the high-energy experimental area, as well as for experiments on the polarizability of nucleons which is currently underway.

In the bypass to the first recirculation the FEL is located. The electron beam

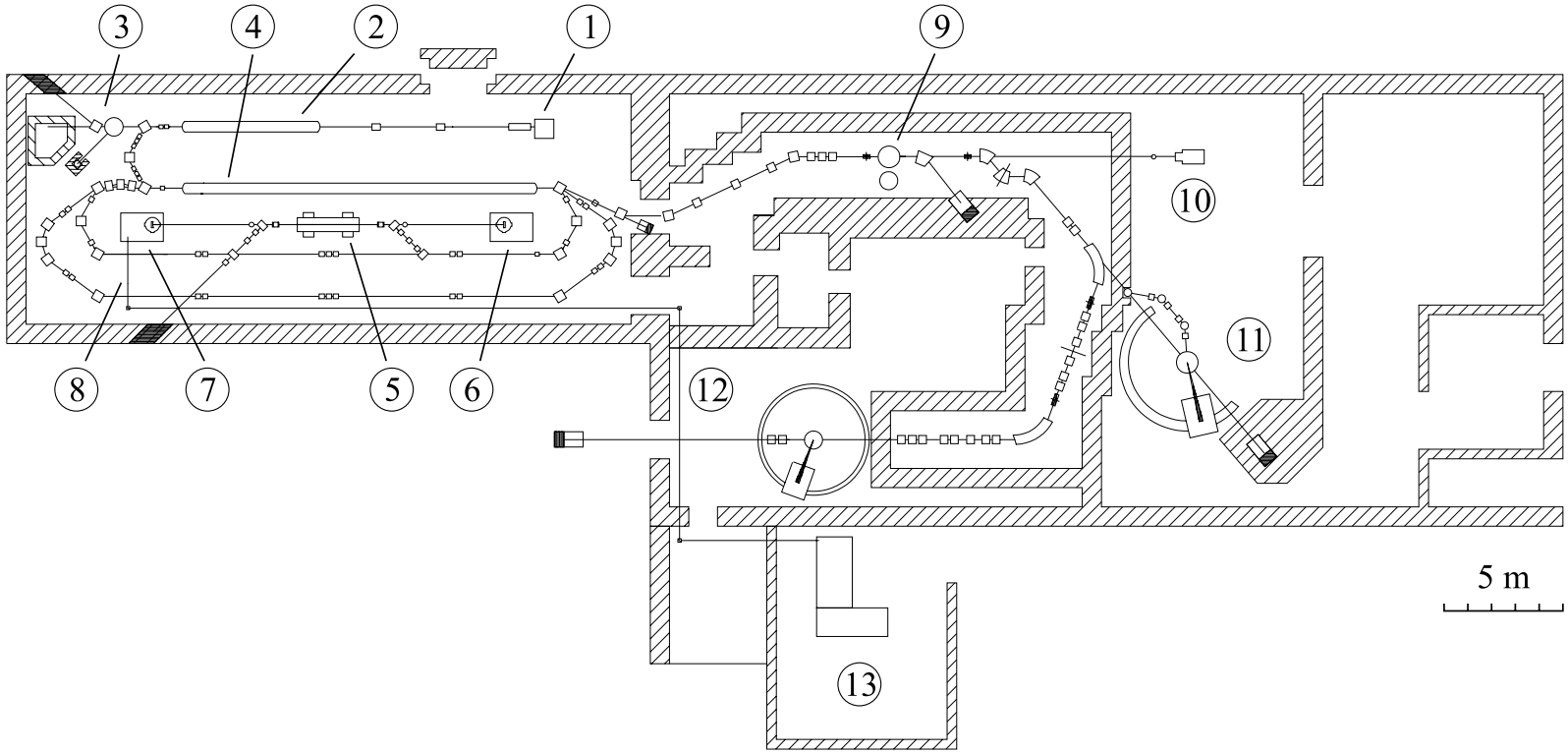

Fig. 4.1: The superconducting Darmstadt electron linear accelerator S–DALINAC: accelerator hall with the FEL (left) and experimental hall (right). (1) electron gun, (2) superconducting 10 MeV injector, (3) experimental area for low energy channelling (LEC), parametric X-ray radiation (PXR) and nuclear resonance fluorescence (γ, γ'), (4) superconducting 40 MeV accelerator, (5) undulator, (6) upstream and (7) downstream tables with mirror chambers, (8) transfer system to the optical laboratory (9) high energy channelling (HEC) and PXR, (10) Compton scattering on the nucleon, (11) QCLAM-spectrometer and bypass-system for electron scattering under 180°, (12) magic-angle spectrometer with the energy-loss system, (13) optical laboratory (located one floor above).

with an energy between 25 and 50 MeV enters a 2.6 m long undulator. The latter is build up from 80 periods each having a length of 3.2 cm and has a variable gap width between 16 and 25 mm. The emitted photon pulses are stored in a 15 m long resonator [43] made out of two concave mirrors having reflectivities of 99.0% and 99.8%, respectively. Inside the undulator the amplification process takes place so, that an infrared laser beam with a wavelength between 3 and 10 μm is generated. The tuning of the wavelength can be reached by varying the electron energy or the undulator gap. The laser beam is extracted by a mirror at the downstream (DS) edge of the FEL. The radiation can be either diagnosed directly on the DS table or can be transported by a 55 m long transfer system to the optical laboratory for further experiments.

Since the amplification of the optical pulse depends strongly on the peak current of the electron bunch inside the undulator, a system of a 10 Mhz sub-harmonic injection was designed and developed [44]. In this case only each 300^{th} high frequency period is filled with electrons but with an increased bunch charge. The bunch length of 2 ps leads to a peak current of 2.7 A which, in turn implies a small signal gain of 2-5%. The time structure of the laser light has the structure of the electron beam and thus, short laser pulses of about 2 ps can be obtained. Because of the utilization of superconductivity in electron acceleration a sequence of micropulses spaced by 100 ns with an arbitrary macropulse duration can be generated.

4.2 Experimental area at the S-DALINAC FEL

Figure 4.2 shows the experimental set-up mounted on the DS table in the accelerator hall. With this set-up both, spontaneous and laser radiation can be diagnosed. The radiation, outcoupled through a multi-layer dielectric mirror (1) can either be transferred to the optic laboratory for further experiments or diagnosed directly at the DS-table. For the diagnostic on the DS-table a system for the measurement of the spectral distribution of spontaneous and stimulated radiation consisting of a monochromator (2) and a nitrogen-cooled HgCdTe-thermo resistor (3) has been developed. The temporary resolution of the detector is about 100 ns so that the

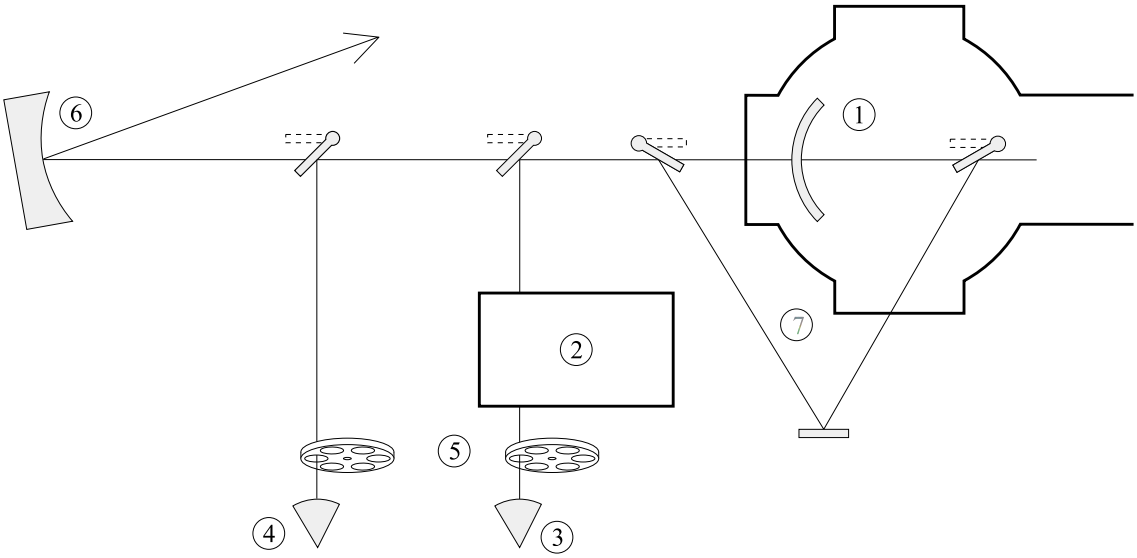

Fig. 4.2: Diagnostic elements on the DS table: (1) Resonator mirror, (2) monochromator, (3) HgCdTe-thermo resistor, (4) set-up for measurement of the total intensity, (5) sets of filters, (6) Transfer telescope, (7) bypass for the spontaneous emission measurements.

intensity evolution within the macropulse can be measured. It should be mentioned that the detector reaches its saturation at a power of about 100 μW. For the measurements above the lasing threshold additional attenuation is necessary. Alternatively the average power can be measured by a thermopile detector (4) which has a temporal resolution of about a few seconds. Two sets of filters (5) are used for the attenuation of the laser radiation or for the harmonics separation. Because of its lower power the spontaneous emission can not be measured after passing through the outcoupling mirror. For this measurement a special bypass (7) has been designed. For the experiments in the optical laboratory the transfer system (6) is used.

4.3 FELIX

The Free Electron Laser for Infrared eXperiments (FELIX) in the Netherlands went into operation in 1991 as the first infrared FEL to obtain lasing in Europe.

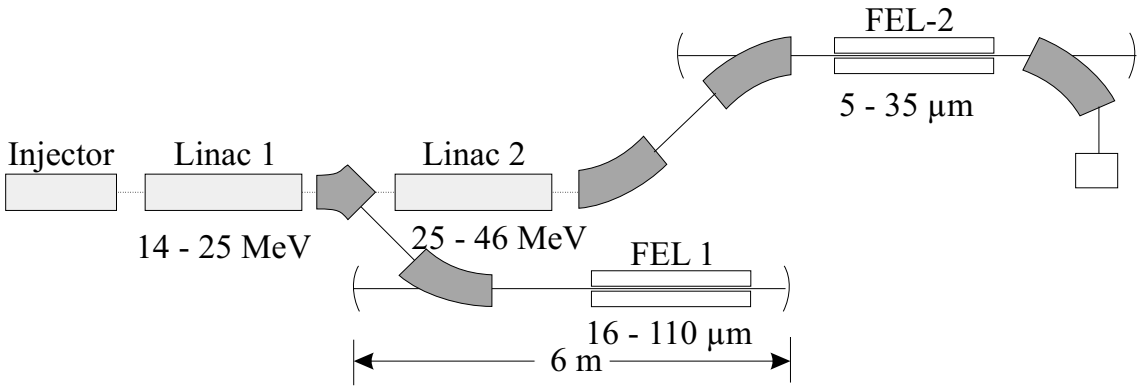

Fig. 4.3: Layout of FELIX.

Figure 4.3 presents an overview of the FELIX layout. An electron beam with an energy of 3.8 MeV is produced by the injector. Two 3 GHz normalconducting linacs are used to increase the beam energy to 15-25 MeV and 25-45 MeV, respectively. Behind each linac the electron beam consists of a train of 3 to 6 ps long bunches and can be bent into an undulator. Both undulators 38 periods of 65 mm length. Two gold-coated mirrors are placed at opposite sides of the undulator and define the 6 m long resonator. This allows to obtain 40 independent micropulses in the cavity simultaneously. An aperture in the left-hand side mirror provides outcoupling of a fraction of optical radiation. The position of the right-hand sided mirror can be adjusted in order to synchronize the circulating optical pulses with electron bunches. Behind the undulator, the electrons are bent out of the resonator and dumped. The laser typically provides several kW of average output power during the macropulse, with a maximum of 20 kW, corresponding to a micropulse energy of 20 μJ.

Table 4.1 summarizes the main parameters of the S-DALINAC FEL and FELIX.

4.4 Experimental set-up at FELIX

The FELIX laser beam providing wavelengths in the region between 5.7 and 9 μm was delivered to the experimental hall through an evacuated transfer system. The wavelength has been tuned by changing the undulator gap keeping the electron energy fixed at 43.6 MeV. The experimental set-up is shown in Fig. 4.4. Colinearly

Tab. 4.1: Parameters of the S–DALINAC IR FEL and FELIX

Parameter	S-DALINAC	FELIX
Electron energy (MeV)	25 – 50	14 – 46
Energy spread (%)	< 0.3	0.2
Electron peak current (A)	2.7	27
Undulator period length (cm)	3.2	6.5
Number of periods	80	38
Undulator parameter K	0.45 – 1.12	< 1.9
Wavelength (μm)	3 – 10	5 – 110
Optical resonator losses (%)	0.9	5 – 10
Resonator length (m)	15.00	6.15
Repetition rate (MHz)	10	1000 (25)
Macropulse duration (μs)	2000 – cw	< 15

propagating to the FEL beam (1), a HeNe-laser beam (2) was used for adjustment of the measuring devices during the experiment preparation. Propagating along the optical table, the FEL beam can be directed either to a second-harmonic autocorrelator (3) designed in [45] or to a monochromator (4) with the help of flip-mirrors (5). Using the monochromator and putting behind it a HgCdTe-thermo resistor (6) it was possible to measure the time-resolved spectral distributions of the FEL within the macropulse.

Some results of these measurements are presented in Sect. 7.2.

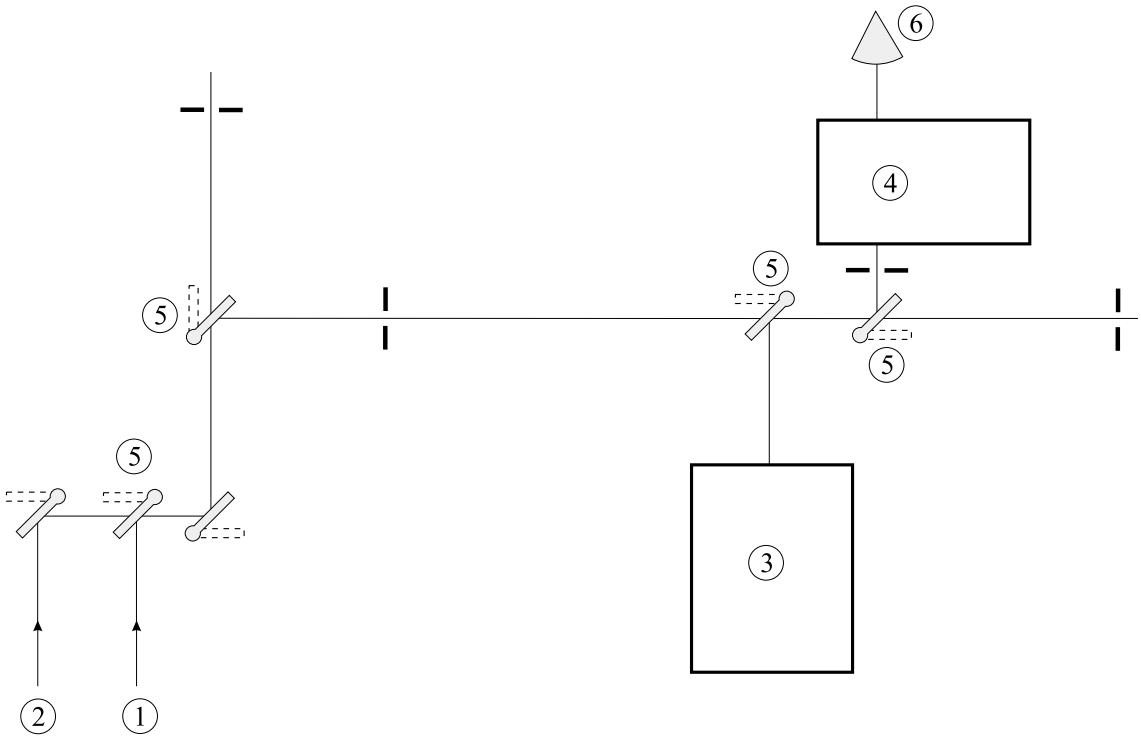

Fig. 4.4: Experimental set-up at FELIX. Colinearly propagating to the FEL beam (1), a HeNe-laser (2) was used for adjustment of the measuring devices during the experiment preparation. Propagating along the optical table, the FEL beam can be directed either to a (3) second-harmonic auto-correlator or to a monochromator (4) with the help of flip-mirrors (5). Using the monochromator and the HgCdTe-thermo resistor behind it (6) it was possible to measure the time-resolved spectral distributions of the FEL within the macropulse.

5 Numerical simulation algorithm

To model the FEL oscillator and its light output, the equations of the electron motion (2.3) - (2.5) have to be solved together with Maxwell's equation (2.21) taking into account the boundary conditions for the electron beam and for the electromagnetic radiation. It is assumed that the lasing process starts from the shot noise in the electron beam. The linear regime of the FEL operation (the small signal regime) has been described analytically (Chap. 2). For the description of the non-linear regime when the FEL reaches saturation, which is the subject of interest of the present work, it was necessary to use numerical methods. Therefore, in Sect. 5.1 a simulation code will be introduced and in Sect. 5.2 the limitations of this simulation code are discussed.

5.1 Description of the simulation code

The simulation code FEL1D-OSC has been originally designed by E. L. Saldin, E. A. Schneidmiller and M. V. Yurkov [22] for the numerical study of the FEL amplifier. For the special purposes of this work the code was extended by the authors to the conditions of the multi-pass Darmstadt FEL. It is a one-dimensional time-dependent code which allows to study the time evolution of the FEL oscillator with variable undulator parameters from the shot noise up to saturation.

The code is based on several simplifying assumptions about the properties of the electron beam and of the electromagnetic field:

- The undulator is placed between two plane parallel mirrors.
- The amplified wave is a plane wave.
- The electron beam has a uniform density distribution in the direction perpendicular to the undulator axis.
- Electrons move along identical trajectories parallel to the undulator axis.

The FEL oscillator is considered as an FEL amplifier with feedback. The electromagnetic wave travels in the resonator forward and backward, reflected by two mirrors. When the wave travels in the same direction of the electron beam, it is amplified due to the beam-wave interaction inside the undulator. The small signal gain (2.32) per resonator pass is assumed to be small.

The resonator is considered to be a Fabri-Perot resonator equipped with two plane parallel mirrors. The distance between the mirrors is equal to L and can be varied by the distance ΔL measured in units of the optical wavelength λ_r. An undulator of length L_u is placed in the middle of the resonator and its axis coincides with the resonator axis. The coordinate of the upstream entrance of the undulator is chosen to be $z = 0$. The electrons move along the planar trajectories in parallel to the $z-$axis (on the average over the undulator period). The angle $\theta_{\max}$ derived from (2.11) is considered to be small and the longitudinal electron velocity v_z is close to the velocity of light ($v_z \simeq c$). The electromagnetic field inside the resonator is assumed to be linearly polarized because of the planar magnetic field of the undulator (2.1).

To calculate the evolution of the radiation in the FEL oscillator two processes have to be taken into account: (i) amplification of the electromagnetic wave by the electron beam and (ii) losses in the mirrors. The electron beam is simulated by N macro particles per interval $(0, 2\pi)$ over the phase ζ.

The procedure of the numerical simulation is organized as follows. At time t_i the unmodulated electron beam appears at the undulator entrance. Simultaneously the electromagnetic field with the amplitude u and phase ϕ enters the undulator.

The equation of motion (2.3 - 2.5) and the wave equation (2.27) are solved numerically by the Runge-Kutte technique integrating over τ in the limits of $\tau = 0$ and $\tau = 1$. After one undulator pass the increase of the field amplitude Δu and its phase $\Delta\phi$ are calculated. Then after the round trip of the radiation in the resonator, i.e. at the moment of time $t_{i+1} = t_i + 2L/c$, the following initial conditions at the undulator entrance are obtained.

The phase change of the electromagnetic field after the reflection from the resonator mirrors is neglected because this effect does not influence the FEL-oscillator operation [25]. The multiple use of this procedure for the given initial conditions at $t_0 = 0$ allows one to calculate the field evolution in time.

For the tapered undulator the same assumptions and definitions of variables are made, but it is taken into account that the detuning parameter is a function of the particle coordinate τ inside the undulator (see Sect. 3.4).

5.2 Limitations of the simulation code

Besides the assumptions discussed in Sect. 5.1 there are several other reasons which limit the application of the code. Since the underlying model is one-dimensional, the interactions seriously modifying the transverse Gaussian profile of the electron or optical beam are not taken into account. The code is valid only for an optical mode which has a waist larger than the electron beam radius, which is the case for the Darmstadt FEL (see Fig. 6.1). For FEL oscillators with high gain the optical field is strongly deformed since the radiation of the electron beam is almost as strong as that inside the resonator. Thus, for the case of a high gain FEL a 3D model should be used to describe satisfactorily the FEL behavior. In case of the Darmstadt FEL the gain is limited to about 5% which allows a 1D treatment. Short-pulse effects are largely longitudinal in nature and that is why the FEL can be modelled adequately in a 1D approximation. The hole-coupling of the optical beam which is often used in FELs also deforms the optical field inside the resonator [47]. To study the FEL dynamics in a hole-coupled FEL the 3D code is preferable. The Darmstadt FEL, however, uses multi-layered partially reflective mirrors which simplifies this task. However, the results presented in Sect. 7.2 show a satisfactory agreement between the results of the 1D simulation and the experiment carried out at FELIX which uses hole-coupling for the extraction of the optical beam.

6 Adjustment of the simulation parameters

Within the framework of the simulation code the output characteristics of the FEL oscillator are functions of the input parameters listed in the Table 6.1.

Some of these parameters are defined by the design of the FEL and by the parameters selected in the experiment. Others are not known accurately enough and difficult to determine experimentally. These parameters are treated as free parameters within the framework of the code employed in this thesis. In the following the reasonable range of these parameters is discussed.

The electron energy E_e, energy spread $\Delta E_e/E_e$ and electron peak current I are defined by the experimental conditions. Since the Darmstadt FEL is driven by a superconducting linac, the accuracy of the energy and peak current values is

Tab. 6.1: Input variables used by the simulation code.

Electron energy (MeV)	E_e
Energy spread (%)	$\Delta E_e/E_e$
Electron peak current (A)	I
Undulator period length (cm)	λ_u
Number of periods	N_u
Resonance radiation wavelength	λ_r
Optical resonator losses (%)	σ
Macropulse duration (round-trips)	T
Tapering depth	α
Cavity desynchronization	$\Delta L/\lambda$
Filling factor	F
Electron bunch length	σ_z
Time integration window	N_{boxbun}

relatively high compared to room-temperature accelerators. The energy spread was measured by means of optical transition radiation and was found to be about 0.3% for the energy range of 25-50 MeV. The undulator period length λ_u and the number of periods N_u, which are both design parameters, together with the electron energy and known peak magnetic field define the resonance wavelength λ_r (see Eq. 2.17).

The losses σ of the optical resonator were precisely determined by measuring the decay of the spontaneous emission intensity stored in the cavity [36] and are equal to 0.83%.

The tapering parameter α is calculated using the definition (Sect. 3.4). The maximum magnetic field amplitude $|B_{\max}|$ is a function of the cavity gap. It was measured [46] and has the form of $|B_{\max}| = 19041.35 \cdot \exp(-0.1017048 \cdot h)$, where $B_{\max}$ is in Gauss and h is the undulator gap measured in mm. The accuracy of the gap adjustment determined by means of the system based on Linear Variable Differential Transducers [21] is about 0.01%.

The active cavity-length stabilization designed in [21] allows to keep the cavity length constant within an accuracy of about 230 nm (FWHM) for a long time (few hours). However, since the absolute zero value of the cavity desynchronization $\Delta L/\lambda$ is not known exactly the cavity desynchronization is treated as a free parameter.

The filling factor F is defined as the ratio of the electron beam cross section divided by the cross section of the optical mode, $F = \pi r_b^2/\pi r_w^2$, where r_b and r_w are electron beam and optical waist radii, respectively. It describes the overlap between the optical mode and the electron beam. The optical waist radius r_w can be calculated analytically for a given resonator configuration and radiation wavelength. For the FEL of the present resonator configuration and the radiation wavelength of 7 μm the waist radius of the optical mode corresponds to 2.46 mm. The radius of the TEM_{00} mode of the resonator at the undulator edges amounts to 2.72 mm. For technical reasons it is quite demanding to measure the radius of the electron beam inside the undulator. A numerical simulation using the code TRANSPORT [49] yields a value of about 0.5 mm (Fig. 6.1) for the electron beam radius. The figure shows also that inside the undulator the typical values of the beam radius vary between 0.3 and 0.8 mm. This results in the variation of the

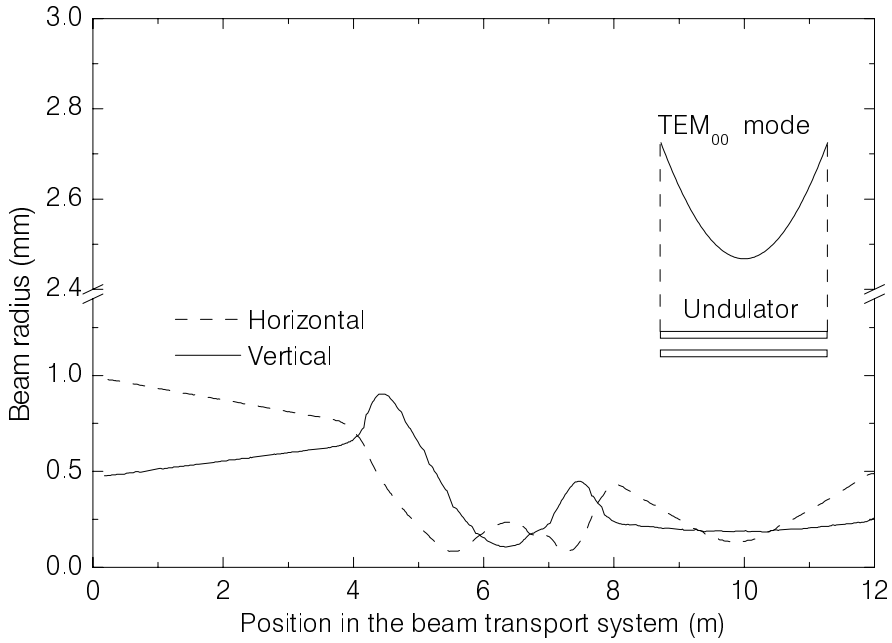

Fig. 6.1: Behavior of the beam envelopes at the energy of 50 MeV inside the beam transport system of the first recirculation (see Fig. 4.1) to the end of the undulator, simulated [49] by the code TRANSPORT. The profile of the TEM_{00}-mode has been calculated analytically.

filling factor between 0.012 and 0.105. For an accurate analysis, however a more precise knowledge of the filling factor F is desirable. Therefore, the filling factor is treated as a free parameter within the given range.

The influence of the finite length of the electron bunch σ_z on the development of the macropulse can not be estimated analytically (see Sect. 2.7) and has thus been studied numerically using the simulation code FEL1D-OSC, described in Sect. 5. The development of the macropulse was simulated for different electron bunch lengths σ_z within the typical range of few ps, keeping all other input parameters of the simulation fixed. The evolutions of the optical pulses during the first 10000 round trips in the cavity for some values of the electron bunch lengths between 0.3 mm (1 ps) and 0.7 mm (2.3 ps) are shown in the left hand side Fig. 6.2. It becomes apparent that the shorter the electron bunch is, the faster the macropulse grows and the higher saturation power it has. Furthermore, the influence of the electron bunch length on the saturated power was analyzed. The right hand side of Fig. 6.2 shows the power at saturation as a function of the

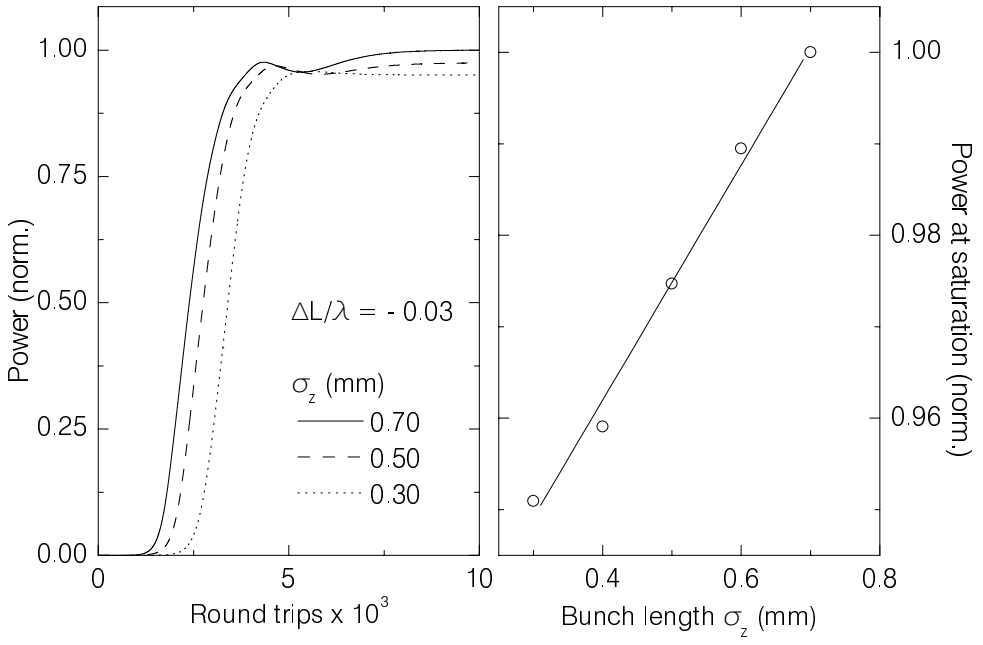

Fig. 6.2: Optical macropulse evolution for different electron bunch lengths (left) and the power at saturation for different values of σ_z (right).

bunch length. Open circles correspond to the power at the end of the macropulse shown in the left hand side of Fig. 6.2. The solid line is a linear fit to the results of the simulation. From the slope the sensitivity of the saturated power on the pulse length can be estimated. It amounts to $12\%/mm$. The electron bunch length σ_z was measured [50] using a Martin-Puplett interferometer. At an electron energy of 30.4 MeV the electron bunch has a duration of (2.0 ± 0.03) ps at FWHM. This corresponds to a bunch length of (0.60 ± 0.018) mm. The influence of the electron bunch length uncertainty reflects itself on an error of the output saturation power of about 0.22% and can thus be neglected.

The N_{boxbun} parameter is a technical parameter of the simulation code. It defines the width (in units of the optical wavelength λ_r) of the time window in which the integration takes place. The window travels with the electromagnetic wave with a velocity c. Its length has to be selected so that it exceeds the electron pulse length in order to take the slippage into account. On the other hand an unreasonable increase of the window length significantly increases the computation time. The influence of the N_{boxbun} parameter on the pulse evolution has also been investigated in the framework of this thesis using the code FEL1D-OSC. The results are

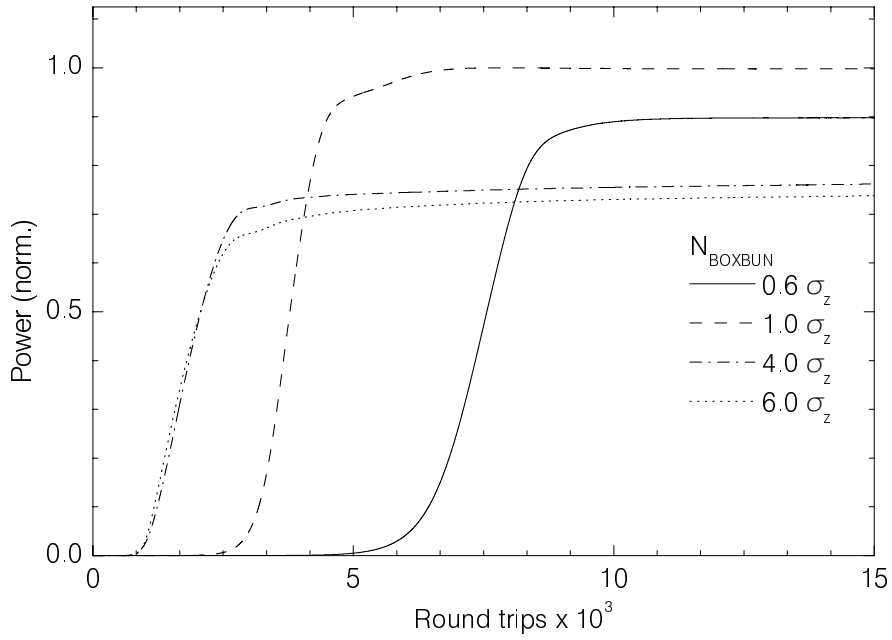

Fig. 6.3: Pulse evolution for different values of the time-integration window. The simulation for an electron bunch with the length σ_z=0.6 mm and a cavity desynchronization $\Delta L/\lambda = -0.03$ has been carried out using the code FEL1D-OSC.

illustrated in Fig. 6.3.

7 Comparison of the simulation with experiment for a uniform undulator

This chapter summarizes the comparison of the results from the simulations with the experimental results obtained at the S-DALINAC and at FELIX. The comparison includes the investigation of the macropulse power, the small signal gain and the spectral distribution.

7.1 Measurements at the S-DALINAC

The experimental data analyzed in this section were obtained [21] at the S-DALINAC. A pulsed electron beam with the macropulse length of 4 ms, a repetition rate of 31 Hz and an energy of 31.04 MeV was used. Together with the undulator parameter $K = 1.106$ this results in the resonant wavelength of 7.03 μm. Figure 7.1 shows

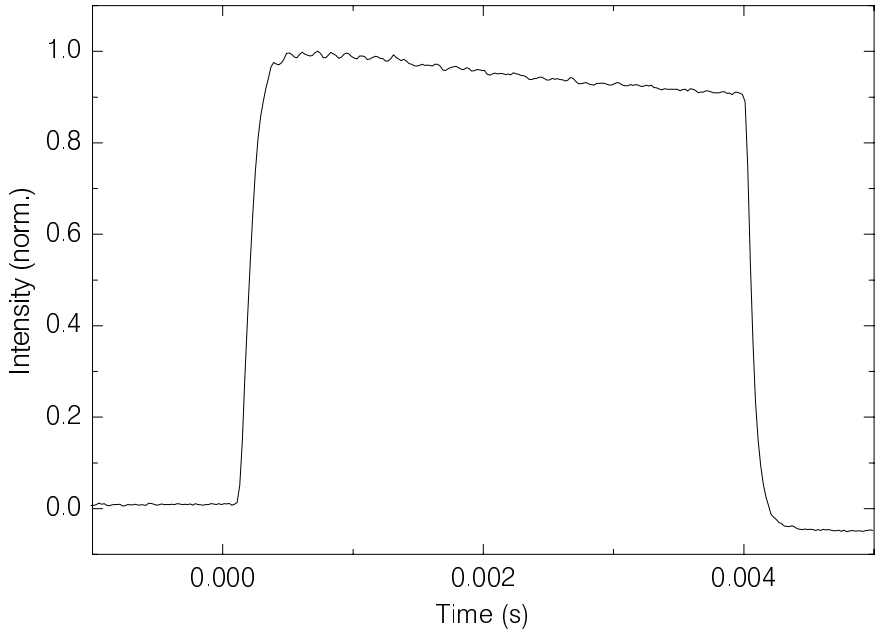

Fig. 7.1: Typical time-resolved macropulse intensity measured at the S-DALINAC. The pulsed electron beam had an energy of 31.04 MeV, a pulse length of 4 ms and a repetition rate of 31 Hz.

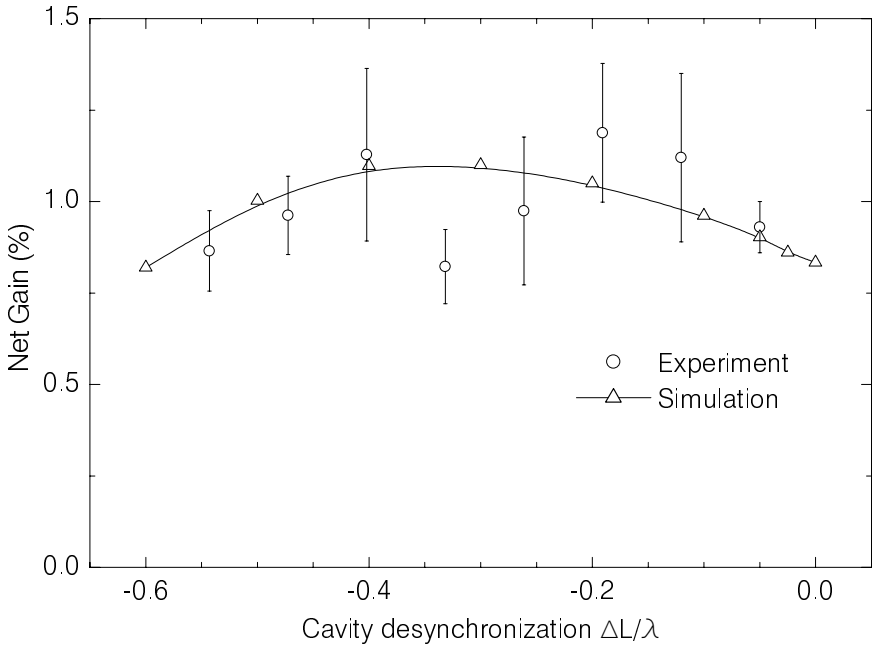

Fig. 7.2: Small signal gain as a function of the cavity desynchronization. Open circles represent the experimental results obtained at the Darmstadt FEL with the beam parameters being identical to those listed in Fig. 7.1. Open triangles are determined by the simulation. The solid curve connects the data from the simulation. Good agreement between experiment and simulation is observed.

an example of the time-resolved laser power development within the macropulse. Saturation of the laser power was reached within the first 400 μs. Time-resolved power measurements were carried out for various cavity desynchronizations, five times for each setting. From the initial portion of the macropulse the information about the small signal gain can be extracted. To reduce the error, the following procedure was chosen for each cavity setting. First, the time was converted into the number of the resonator round-trips. The leading edge of the macropulse was then plotted on a logarithmic scale and a linear function $y_i = a_i + g_i t$, $i = 1 \ldots 5$ was fitted to the linear regime. For the values of g_i with the corresponding errors σ_i^2 the weighted mean $\hat{g} = \sum_{i=1}^{5} (g_i/\sigma_i^2) / \sum_{i=1}^{5} (1/\sigma_i^2)$ has been calculated with an error of $\sigma^2(\hat{g}) = 1/\sum_{i=1}^{5} (1/\sigma_i^2)$. The results are presented in Fig. 7.2. The circles with error bars represent the measured data. With the parameters of the

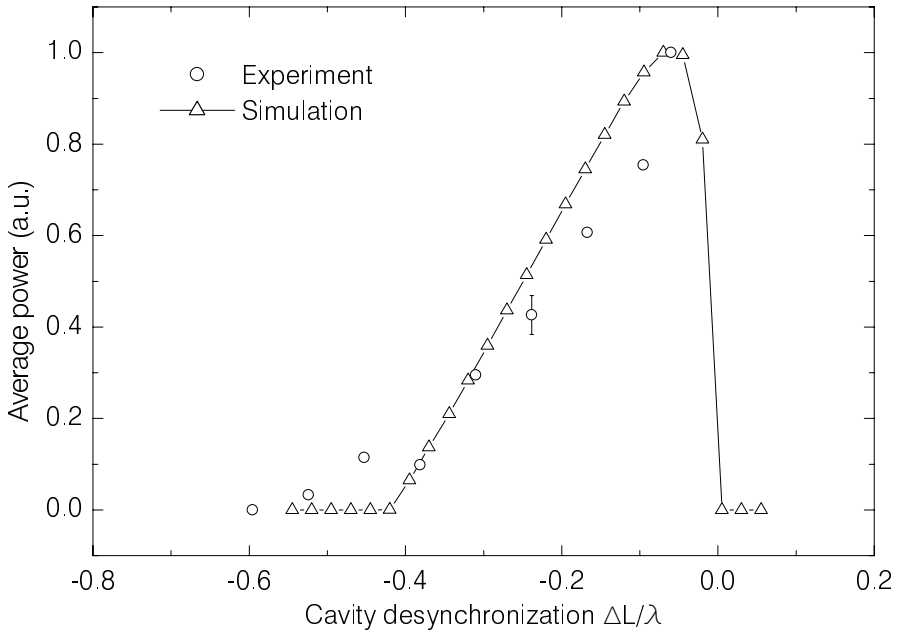

Fig. 7.3: Average macropulse power as a function of cavity desynchronization measured at the S-DALINAC (circles) compared with the results of simulation (solid line). Open triangles show the points for which the simulations were performed.

experiment the evolution of the macropulses has been numerically simulated and the information about the small signal gain has been extracted using the same procedure as for the experimental data. The triangles represent the values of the small signal gain determined by the simulations. The solid line is a fit to the values (triangles) obtained from the simulation code. Good agreement is observed between experimental data and numerical results.

Simultaneously to the time-resolved measurements, the average macropulse power was recorded for each value of the cavity desynchronization by a thermopile detector. In Fig. 7.3 the results of numerical simulation are compared to the results of these measurements, and indeed both are in a good agreement.

Finally, for a cavity desynchronization of $\Delta L/\lambda = -0.05$ the spectral distribution of the radiation was measured at the beginning of the macropulse with the help of monochromator and HgCdTe-detector (see Sect. 4.2). The spectral resolution was 25 nm. The time gate was set for 20 μs which is equal to 200 round trips. Each point was averaged over 31 macropulse. The measured spectral distribution

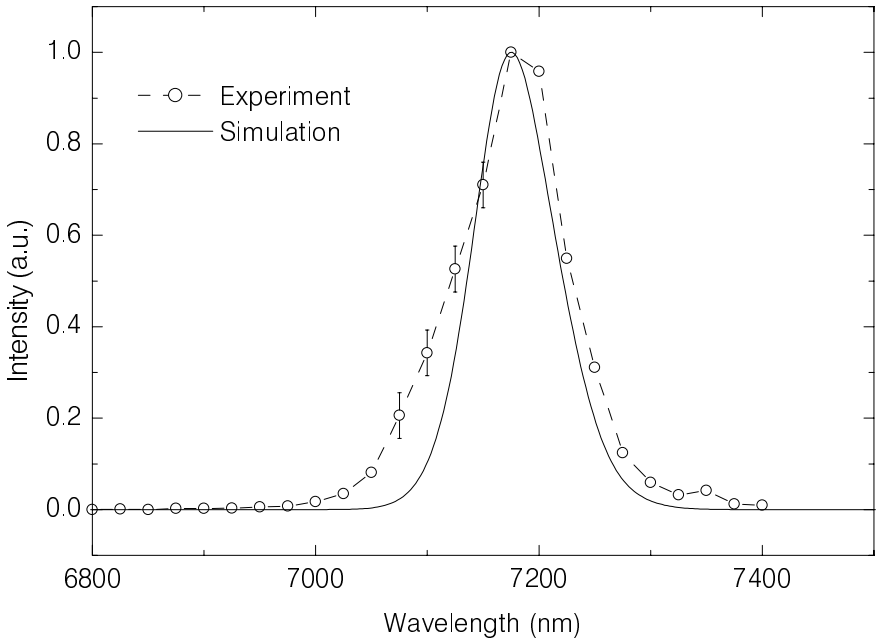

Fig. 7.4: Spectral distribution of the laser radiation measured at the S-DALINAC (dashed line) and the results of simulations (solid line).

(circles) is shown in Fig. 7.4. The spectral distributions obtained numerically were compared to the experimental results. The simulation was carried out for the first 200 round trips and the spectral distributions after each round trip were calculated by a past-processor. All spectral distributions were averaged and the average is shown in Fig. 7.4 as a solid line. The results of the simulation show a smaller line width and are otherwise in fair agreement with experiment. The small deviation *e.g.* at the longer wavelength might result from possible variations of the cavity length, since the measured spectral distribution is averaged over a large number of macropulses. There is also a possibility that the use of a 3D simulation code may explain this discrepancy. Summarizing, it is evident that the numerical simulation reproduce the following experimental data for the Darmstadt FEL with the uniform undulator well: the small signal gain vs. desynchronization, the power vs. desynchronization and the spectral distribution.

7.2 Measurements at FELIX

This section summarizes the comparison of the results of numerical simulations with the experimental results obtained at FELIX. The experimental set-up has been described in Sect. 4.4. Time-resolved spectral measurements were performed. Electrons with an energy of 43.6 MeV were employed. The wavelength of the radiation was set by changing the undulator gap. As has been pointed out above, contrary to the Darmstadt FEL, the FELIX facility is driven by a normalconducting accelerator. This limits the macropulse duration to a few μs and the repetition rate to a few Hz. The results presented here were obtained with a pulsed electron beam having a macropulse duration of 7 μs and a repetition rate of 5 Hz.

Figure 7.5 (top) shows a sample of the measured time-resolved spectral distribution, obtained at the resonant wavelength $\lambda_r = 7.4$ μm with a cavity desynchronization of $\Delta L/\lambda = -0.57$. The data acquisition system was synchronized with the accelerator triggering pulse. The zero position on the time-scale corresponds to the beginning of the macropulse. The electron beam was switched off after 7 μs. The time-resolved spectral distribution (Fig. 7.5, top) was measured in the wavelength range between 6600 and 7880 nm in steps of 20 nm. Laser generation started approximately after 3 μs and at 4 μs FEL reached saturation. Vertical stripes presented on the time resolved spectral distribution were identified as absorption lines of water vapor.

The integration of the time-resolved spectral distribution over the entire spectral range gives the time evolution of the total power which is shown in Fig. 7.5 (middle). One can clearly see the oscillation of power after saturation. This can be explained by the limit-cycle oscillation (Sect. 2.7) since at this wavelength FELIX operates at the short-pulse regime.

The integration of the time-resolved spectral distribution over the entire macropulse duration gives the average spectral distribution of the FEL pulse, which is shown in Fig. 7.5 (bottom). The spectral distribution looks asymmetric with the long tail at the longer-wavelength side which evidently also points to the presence of the limit-cycle oscillations (see Sect. 2.7).

The experimentally observed power evolution presented in Fig. 7.5 (middle) has

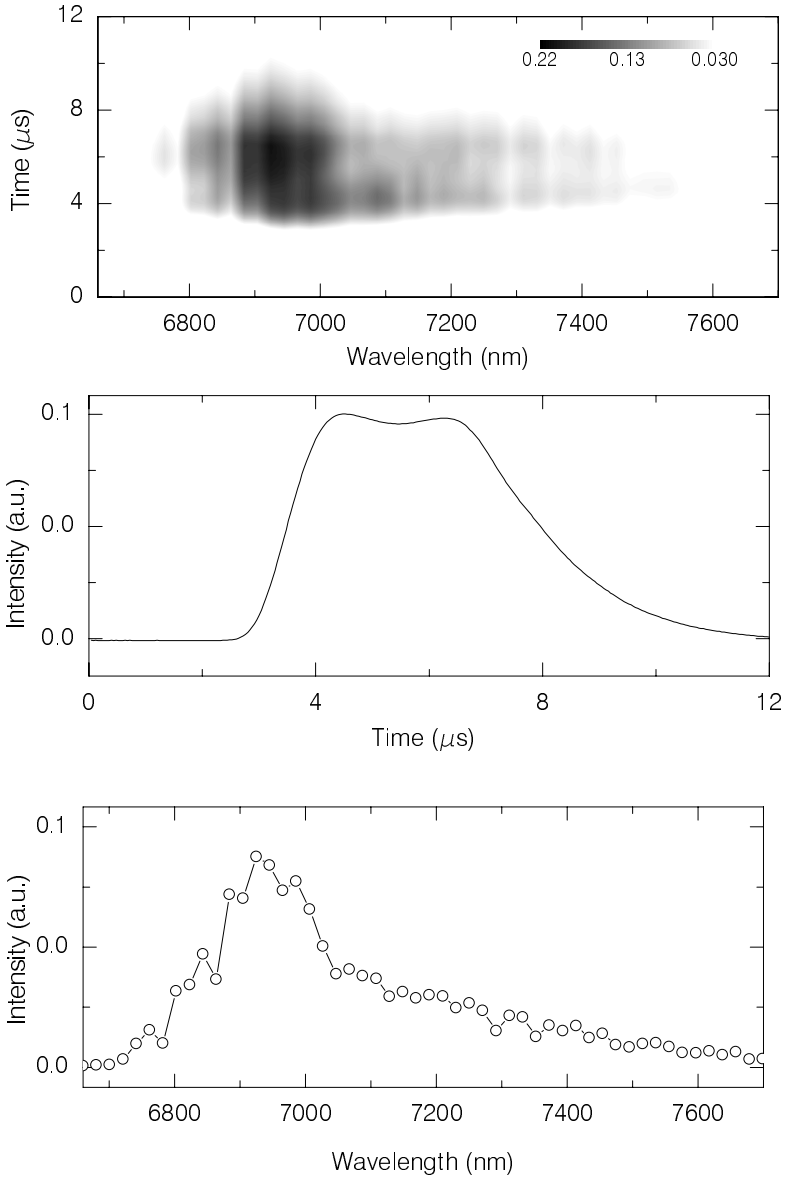

Fig. 7.5: A sample of a time-resolved spectral distribution measured at FELIX (top). The zero position on the time-scale corresponds to the beginning of the electron macropulse. The electron beam was switched off after 7 μs. The total power evolution (middle) is obtained by integration of the time-resolved spectrum over the entire wavelength region. The spectral distribution averaged over time (bottom) is antisymmetric with a long tail at the longer wavelength side which together with the oscillation in the total power evolution points to the limit-cycle regime.

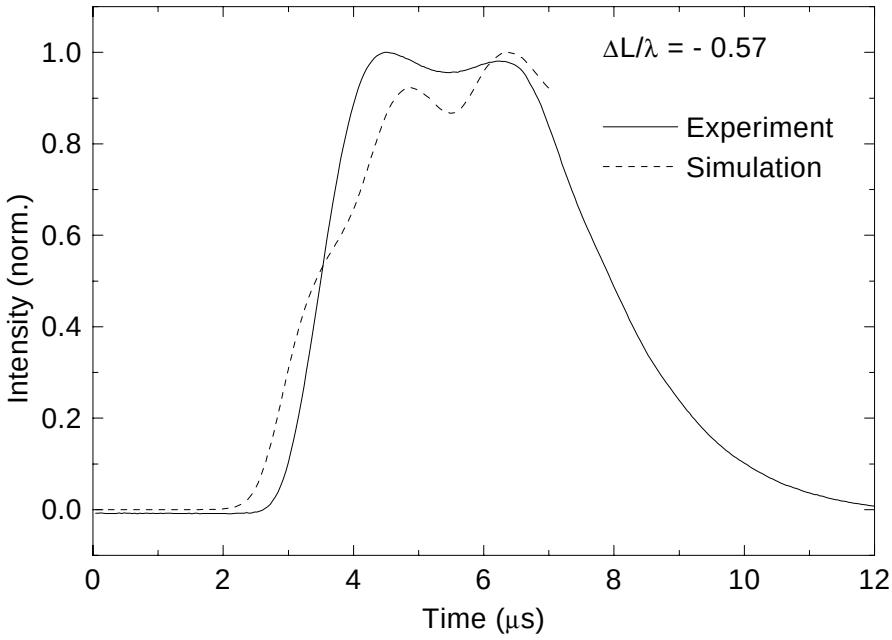

Fig. 7.6: Comparison of the macropulse evolution (solid line) measured at FELIX and its simulation (dashed line). Wavelength $\lambda_r = 7\ \mu m$, cavity desynchronization $\Delta\lambda/\lambda = -0.57$.

been compared to the results of numerical simulations. As input parameters for the simulation the following values were chosen. The main technical parameters of the FELIX FEL are those listed in table 4.1. The optical resonator length of the FELIX FEL amounts to 6.15 m which corresponds to the round trip time of the optical pulse of $4.1 \cdot 10^{-8}$ s. The macropulse with the length of 7 μs consists of 170 full round trips. The micropulse length is equal to 0.4 – 0.6 mm which corresponds to 57 – 85 λ_r. The parameter $N_{boxbun} = 100$ was chosen to keep the integration window equal to the sum of electron bunch length and the slippage distance. A filling factor $F = 0.165$ gives the best value for the small signal gain at which the laser power reaches saturation after approximately 70 round trips. A comparison of the measured power evolution with its simulated results is presented in Fig. 7.6. The results of the simulation (dashed line) agree satisfactorily with the experiment (solid line) with respect to the slope of the macropulse and the time necessary to reach the saturation. Obtained numerically period of the power oscillations corresponds well to that observed experimentally. The more pronounced character of the oscillation in the case of simulation can be explained

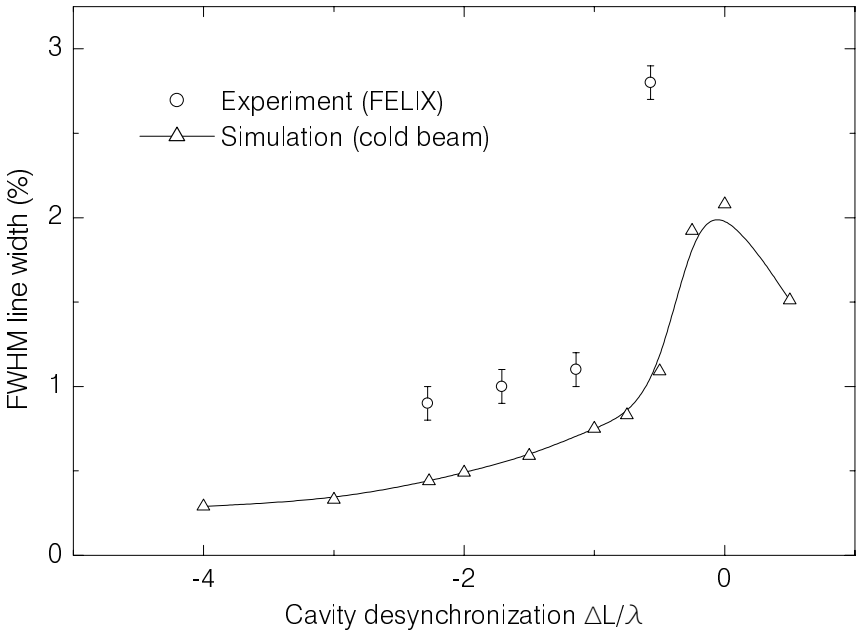

Fig. 7.7: Comparison of the measured (circles) relative spectral width (FWHM) at FELIX with the results of the simulation (triangles) for a cold electron beam for different values of cavity desynchronization.

by the fact that the simulation was performed for a cold electron beam.

As shown in Sect. 2.7, the regime of the operation of the short pulse FEL influences not only the macropulse evolution but also the spectral distribution. In order to study this effect the spectral distributions were obtained for four different cavity desynchronizations similar to that presented in Fig. 7.5. The dependence of the spectral width (FWHM) from the cavity desynchronization is shown in Fig. 7.7. The circles represent the measured values. The triangles, connected by the solid line, correspond to the values obtained by means of numerical simulations. A similar behavior of both experimental data and numerical results is observed. At the same time some discrepancy with respect to the absolute values of the spectral width is noticed. This difference might arise on the one hand from neglecting the energy spread of the electron beam within the simulations and on the other hand from the omission of 3D effects in the model chosen for the simulation code (see Chap. 5.2).

Summarizing this chapter, it should be mentioned that the results of the simulations with the 1D time dependent code are in a good agreement with the results

observed on two different short-pulse FELs in Darmstadt and at FELIX. The dependencies of all main FEL characteristics such as small signal gain, average power and spectral width from the cavity desynchronization correspond well to the experimentally observed ones in the case of a uniform undulator.

8 Data acquisition and results for the tapered undulator

Using the experimental setup described in Sect. 4.2 the spectral distributions of the FEL intensity were measured for seven different tapering parameters α. The applied cavity desynchronization was adjusted by maximizing the output power for each value of the tapering depth. Figure 8.1 shows a typical distribution of the output signal of the HgCdTe-thermo resistor (Fig. 4.2) as a function of the wavelength. Measurements were performed in the range between 6700 and 7400 nm in steps of 5 nm. The detector signal had negative polarity and thus, was inverted for further processing. The zero-level has been chosen as the mean value in the intervals $6700 - 6850$ nm and $7150 - 7400$ nm and was subtracted. A typical spectral distribution of the intensity is displayed in Fig. 8.2.

Between the output mirror and the detector the laser light was transported through the air. Therefore, the spectral distribution is distorted in this wavelength region because of the absorption by water vapor in the atmosphere. The exact density of the vapor "target" is not known. The dashed curve shows the

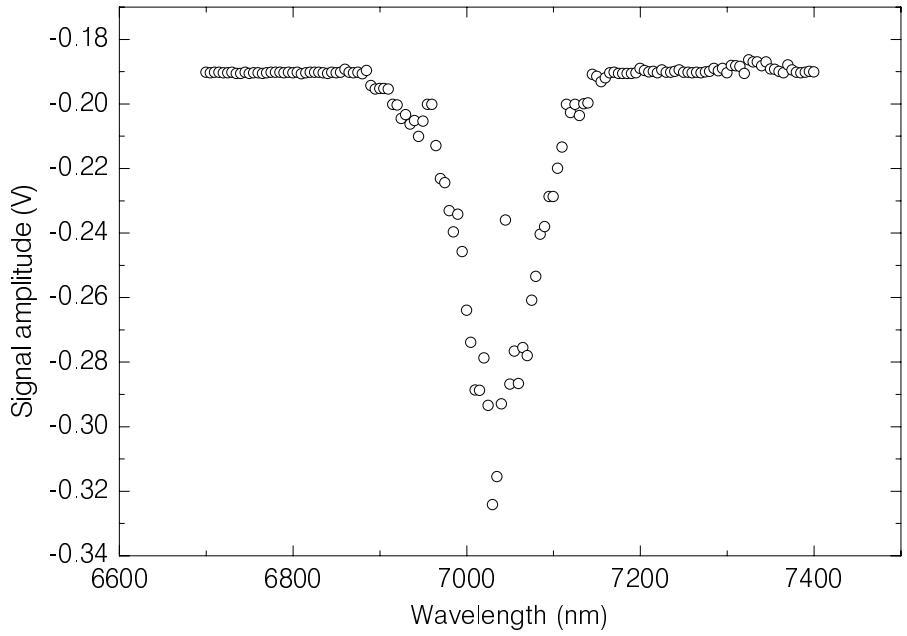

Fig. 8.1: Typical output signal of the HgCdTe-thermo resistor (Fig. 4.2) as a function of the wavelength.

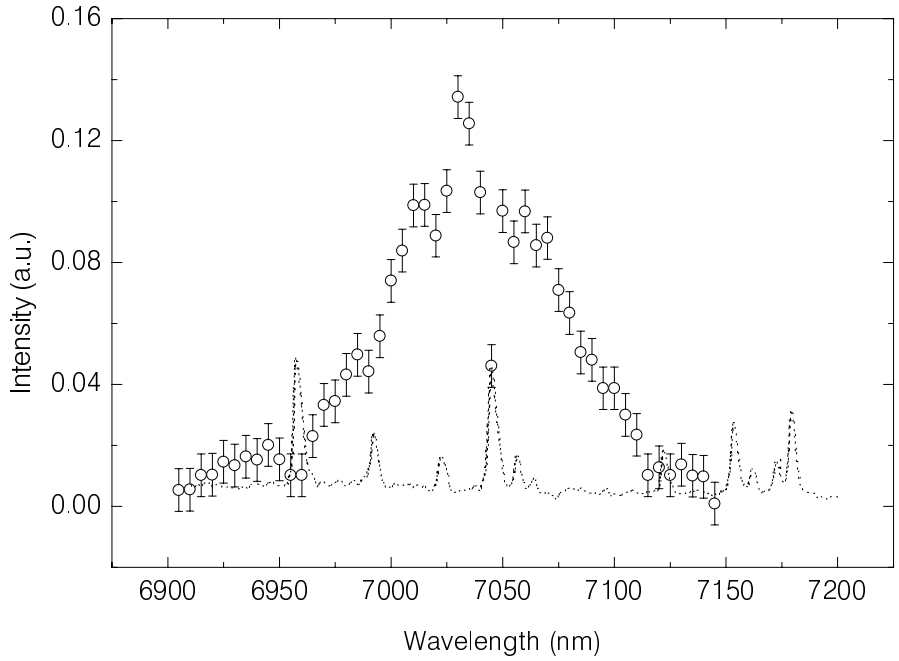

Fig. 8.2: Measured spectral distribution for a uniform undulator (circles) and absorption spectrum of water vapor (dotted line).

absorption spectrum of the water vapor [51] in arbitrary units. It becomes apparent that within the considered spectral range, the probability of absorption is almost constant, except for several narrow maxima. The corresponding lines in the absorption spectrum have a FWHM of less than the step size of the monochromator. A correlation between the positions of the absorption maxima and the position of "holes" in the spectral distribution is observed. Therefore, the six points around the absorption maxima were ignored for further processing and it was assumed that the decrease of the intensity in the remaining spectral region was constant and did not influence the spectral shape.

For further processing of the data, an expression $E(\lambda)$ of the following form

$$E(\lambda) = a + b \exp\left[\frac{-(\lambda - c)^2}{d^2}\right] \tag{8.1}$$

was fitted to the data points, where a describes the signal off-set, b is proportional to the maximal intensity value, c defines the position of the maximum, and d corresponds to the width of the spectral distribution. All measured spectral distributions and the least square fits are shown in Fig. 8.3. For comparison, the

Tab. 8.1: Parameters obtained by fitting the function of Eq. (8.1) to the spectral distributions measured for different values of tapering depth α.

α	$a \pm \Delta a$	$b \pm \Delta b$	$c \pm \Delta c$	$d \pm \Delta d$	χ^2
-16.48	0.007 ± 0.003	0.061 ± 0.004	7004.8 ± 1.3	24.7 ± 2.1	0.24
-14.14	0.002 ± 0.002	0.090 ± 0.003	7011.9 ± 1.1	41.5 ± 2.1	0.49
-9.44	0.008 ± 0.002	0.126 ± 0.003	7018.5 ± 0.9	53.5 ± 1.9	1.31
-4.73	-0.002 ± 0.004	0.120 ± 0.004	7026.6 ± 1.1	82.1 ± 3.5	1.58
0.00	0.008 ± 0.002	0.108 ± 0.003	7036.2 ± 1.0	52.3 ± 2.1	0.78
4.74	0.018 ± 0.002	0.098 ± 0.003	7046.4 ± 1.1	55.5 ± 2.4	1.55
9.50	0.010 ± 0.002	0.094 ± 0.003	7069.1 ± 1.2	56.2 ± 2.3	1.53

absorption spectrum of water vapor is plotted below each spectrum. The parameters, deduced from the analysis and their errors as well as χ^2- the squares of the standard deviations are listed in Table 8.1 for seven spectral distributions. The value at $\alpha = 14.35$ has been omitted for the analysis to deduce the fit parameters because the uncertainties of the fitting procedure did not allow to extract precise values of the parameters. This may result from the fact that the signal was too small for this large α value. However, for the determination of the peak power and the efficiency (Tab. 9.1) this data point was taken into account.

The small, close to unity χ^2 values for the majority of the spectral distributions and the small value of the isotropic term a serve as a proof of the Gaussian shape of the measured spectra. The value of the maximum intensity b varies noticeably with α. For two values of α the maximum intensity exceeds the corresponding value for the uniform undulator $\alpha = 0$. With increasing α the center of gravity c of the spectral distribution shifts towards a longer wavelength λ. For the majority of spectral distributions the parameter d, which describes the width of spectral distribution, does not change much with α.

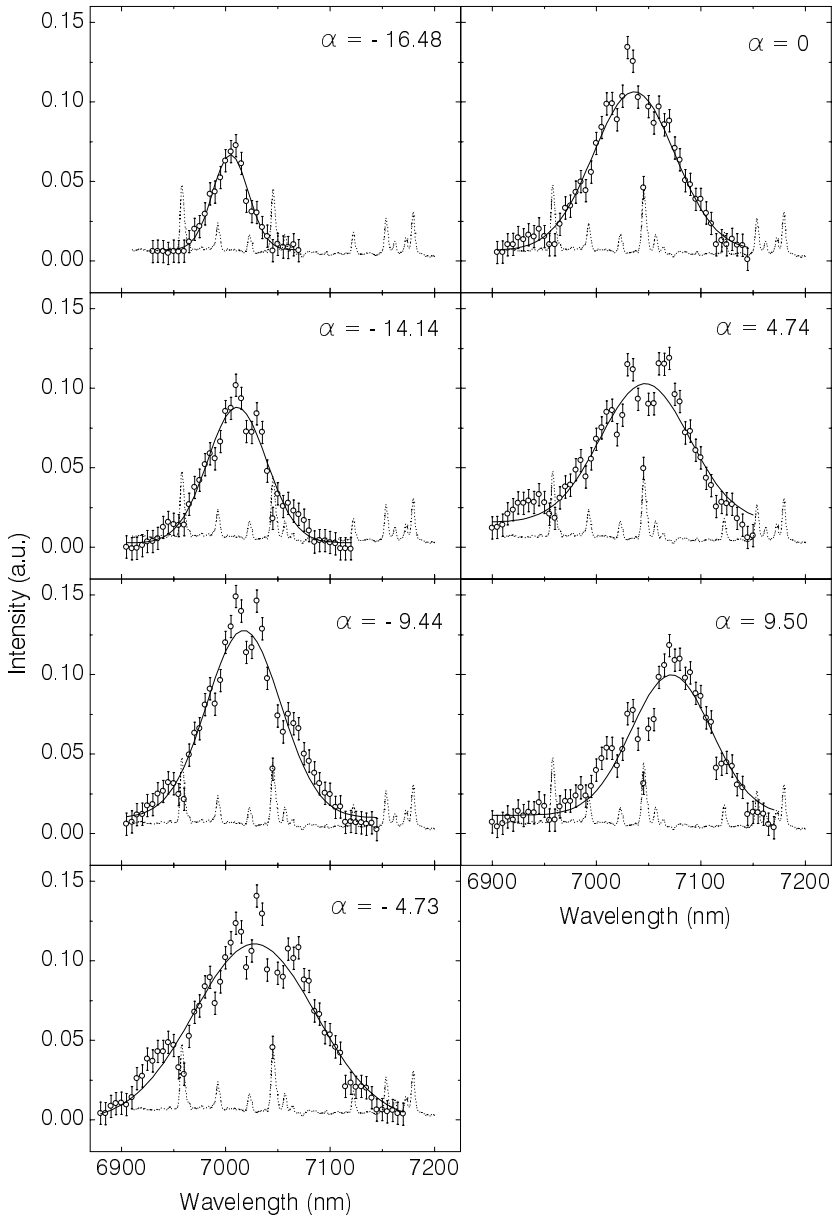

Fig. 8.3: Spectral distributions (circles) measured at the Darmstadt FEL for different tapering depths and a fit (solid line) using the function (8.1). The dashed line represents the absorption spectrum of water vapor.

9 Discussion

9.1 Position of the maximum in the spectral distribution

It has been predicted [11, 23], that the lasing wavelength is determined by the position of the maximum in the spectral distribution of the small signal gain (see Fig. 2.3, top). The position of the maximum in the small signal gain spectrum is a function of the tapering depth (see Fig. 3.4). In the simple case, *i.e.* neglecting the spatial electron beam charge and assuming a continuous beam, it is expected that for a tapered undulator the small signal gain curve can have several maxima depending on α (see Sect. 3.4). The value of the small signal gain at the maximum depends also on the tapering depth. For the described experiment the tapering depths are varied in the range which corresponds to the first maximum. The wavelength shift $\Delta\lambda$ between the lasing wavelength λ and the resonance wavelength λ_r for a uniform undulator, with the value of the undulator parameter K which is equal to the value of K_{in} of a tapered undulator, is predicted to have a form of (see Sect. 3.4):

$$\Delta\lambda = \left[2.6 - \frac{\alpha}{2} - y_1\left(|\alpha|\right)\right] \frac{\lambda_r}{2\pi N_u} \tag{9.1}$$

The positively-defined function y_1 makes a small contribution and depends only on the absolute value of the tapering depth α. Taking into account that $y_1\left(|\alpha|\right) \ll |\alpha|$, then (9.1) can be re-written as

$$\Delta\lambda \approx \left[2.6 - \frac{\alpha}{2}\right] \frac{\lambda_r}{2\pi N}. \tag{9.2}$$

In Fig. 9.1 the circles represent the difference $\Delta\lambda$ between the measured positions of the spectral distribution peaks c and the resonant wavelength of the radiation λ_r for the uniform undulator $\Delta\lambda = c - \lambda_r$. The dashed line shows the result of the calculation using Eq. (9.2). A systematical deviation of the experimental points from the theoretical prediction is observed for all points, except for the uniform case $\alpha = 0$.

The difference $\delta(\Delta\lambda)$ between the experimental values of $\Delta\lambda$ and the calculated results is shown in Fig. 9.2. The solid line represents a linear fit to the first six

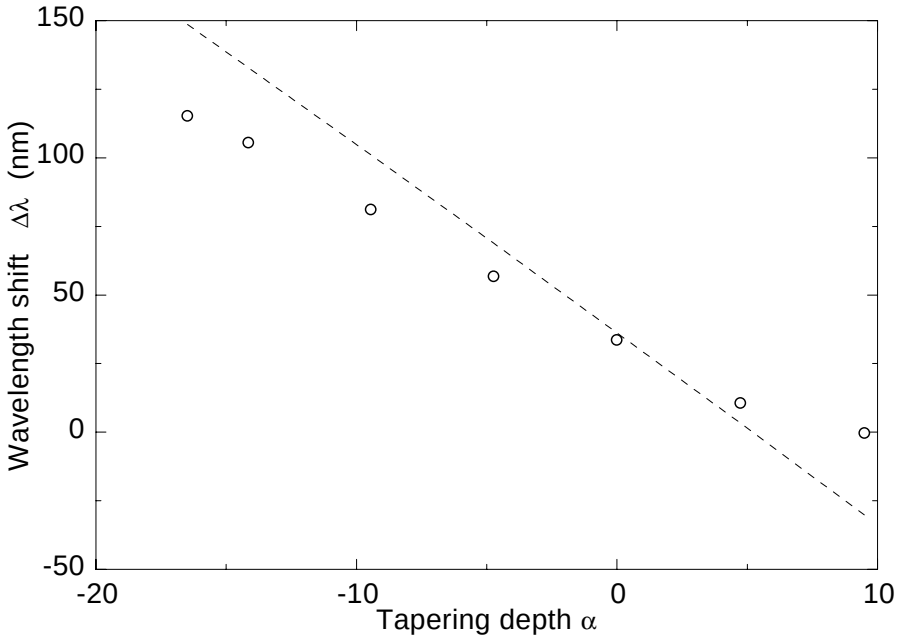

Fig. 9.1: Difference between the experimentally defined position of the spectral distribution peak and the resonant wavelength of the radiation for a uniform undulator (circles) compared to the calculated values (dashed line) using Eq. (9.2).

points with the function $\delta(\Delta\lambda) = 2.82 - 1.84\alpha$. Thus, according to Eq. (9.1) the function y_1 has the form $y_1 = 2\pi N_u \left|\delta(\Delta\lambda)\right| / \lambda_r \approx 1.1 \left|\alpha\right| / 7$. Figure 9.3 shows the function (9.1) using the function y_1 as defined above. Satisfactory agreement is observed only for $\alpha < 0$. For the positive values of the tapering depths there is a considerable disagreement. The relatively large value of y_1 compared to the theoretically predicted value ($y_1 \ll |\alpha|$) from the one hand and the disagreement of the wavelength shift for positive tapering parameter ($\alpha > 0$) from the other hand, show that the observed results can not be explained correctly in the framework of the long pulse approach [11]. Therefore, numerical simulations were performed to define the peak position taking into account the short pulse effects. In Fig. 9.4 the experimentally observed wavelength shift $\Delta\lambda$ (circles) is compared with the results of the numerical simulations (dashed line). A considerable improvement for the positive values of α is observed. The influence of the short pulse effects on the wavelength shift can be explained in the following way. Due to the slippage of the electron beam with respect to the optical pulse the interaction region is

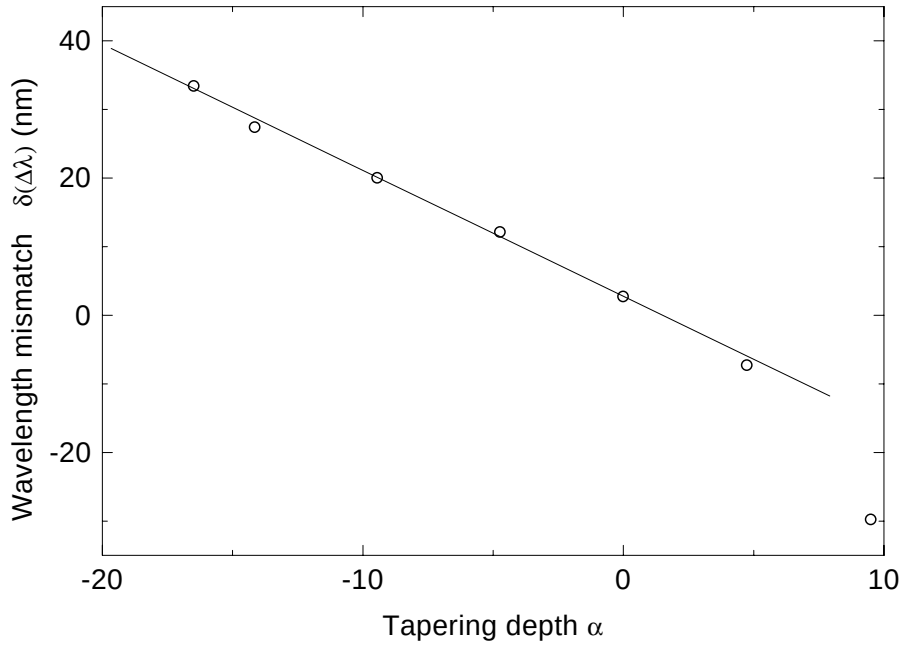

Fig. 9.2: Difference between the experimental results for $\Delta\lambda$ as displayed in Fig. 9.1 and the theoretical predictions according to Eq. (9.2) as a function of tapering parameter α. The solid line represents a fit of a straight line to the first six points.

reduced reflecting in a change of an effective undulator parameter K. This is the reason why the resonant wavelength is somewhat different from that predicted within the framework of the long pulse approach.

In conclusion, it can be stated that the shift of the spectral distribution with the variation of the tapering depth values can not be explained successfully within the framework of the long pulse approach but it is in good agreement with the results of the numerical simulations assuming short pulse effects.

9.2 Spectral width

A fit to the measured spectral distribution using Eq. (8.1) yields the values of the parameter d, which characterizes the spectral width as is listed in table 8.1. The FWHM of the spectral distribution is related to the d parameter according

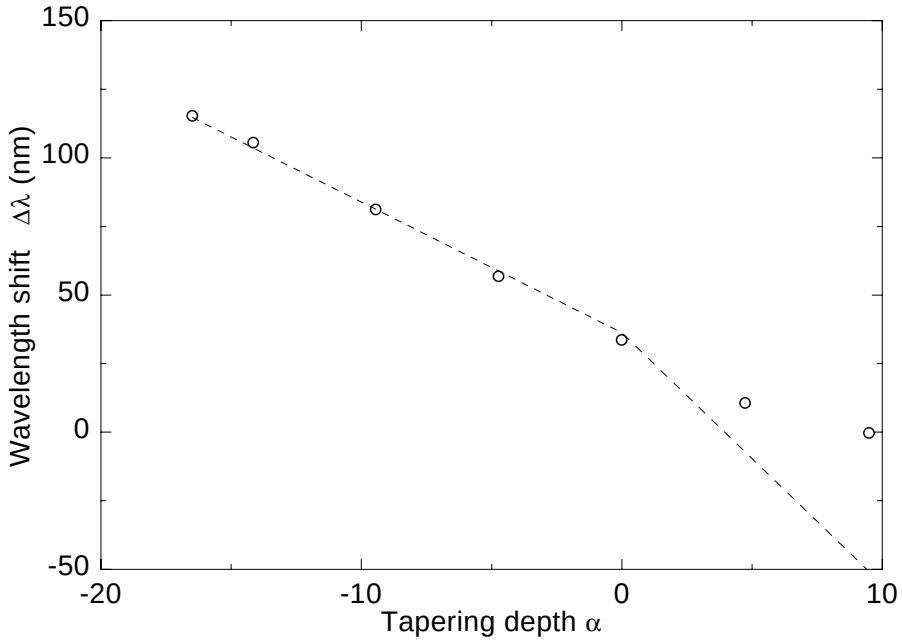

Fig. 9.3: Comparison of the measured wavelength shift (circles) with the calculation using Eq. (9.1), when $y_1 = 1.1\,|\alpha|\,/7$ (dashed line).

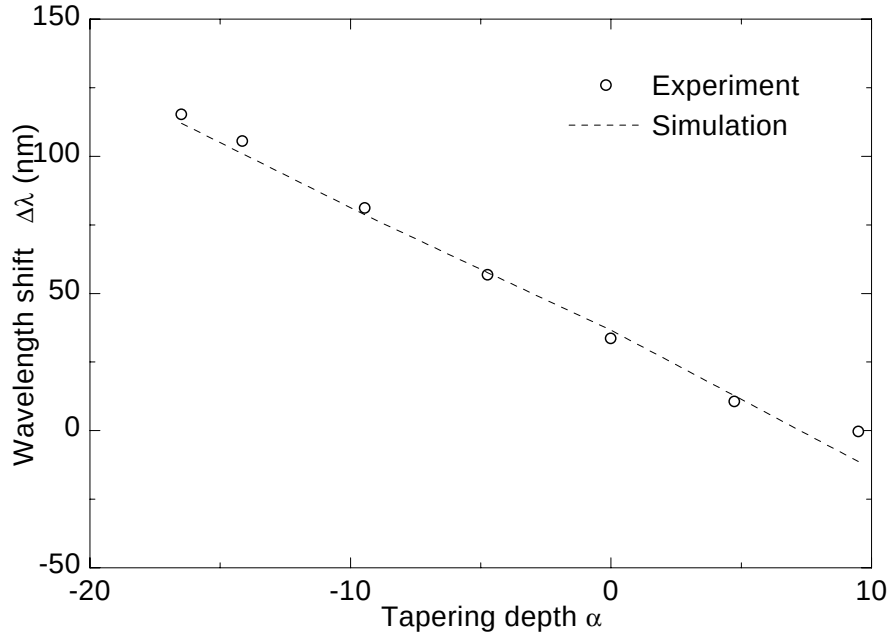

Fig. 9.4: Comparison of the measured wavelength shift (circles) with the results of the numerical simulations (dashed line).

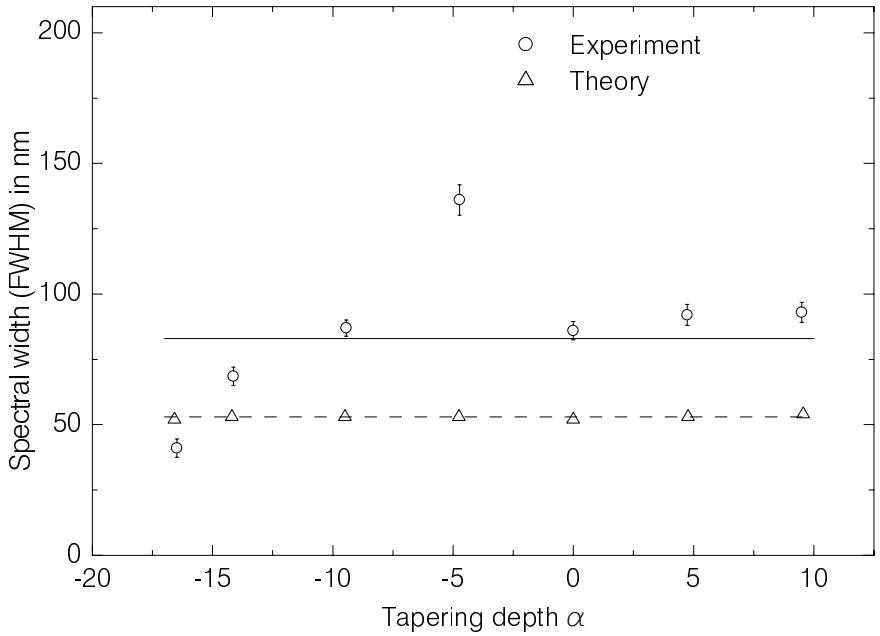

Fig. 9.5: Spectral width (FWHM) as a function of tapering depth. Experimental (circles) and theoretical values obtained using Madey's theorem from the spectral distribution of spontaneous emission assuming a cold electron beam (triangles) compared to the results deduced from the width of the gain curve for the cold beam (dashed line) and for the beam with $\Delta E_e/E_e = 0.3\%$ (solid line).

to $\sigma_0 = 1.65d$. In this Section the influence from different beam parameters on the spectral width is analyzed.

In Fig. 9.5 the circles show the dependence of the spectral width (FWHM) from the tapering depth α as obtained in the experiment. The triangles represent the width of the gain spectrum obtained applying Madey's theorem (see Sect. 2.5) to the spectral distributions of spontaneous emission and assuming the idealistic cold electron beam and "perfect" injection. An essential discrepancy is observed. For real experimental conditions the following improvements should be taken into account, which can possibly explain this discrepancy:

- divergence of the realistic beam
- not "perfect" injection
- energy spread of the electron beam

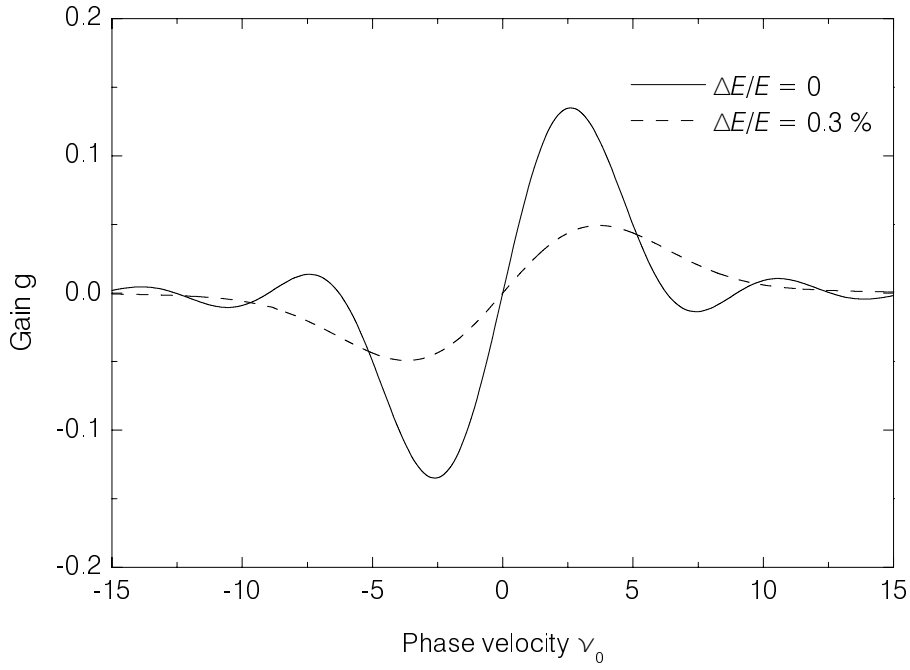

Fig. 9.6: Gain function. Solid line - cold electron beam, dashed line - electron beam with the energy spread $\Delta E_e/E_e$=0.3%.

- broadening of the gain function in strong optical fields

A monoenergetic electron beam can have a random spread in angle consistent with the emittance of the beam. The mean square divergence of the electron beam provided by the S-DALINAC is limited by the value $\langle\theta^2\rangle^{1/2} \leq 3 \cdot 10^{-4}$ rad. In [23] the normalized parameter of the angular spread σ_θ is defined as $\sigma_\theta = 4\pi N\gamma^2 \langle\theta^2\rangle / (1+K^2)$. For the current experiment $\sigma_\theta \leq 0.16$. The dependence of the angular divergence on the gain spectrum in the region of $0 \leq \sigma_\theta \leq 8$ is shown in Fig. 7 of [23]. For such a small parameter no broadening in the gain spectrum is observed. Thus, the angular divergence of the real beam can not explain the spectral broadening observed in the experiment.

An imperfect injection of the electrons, caused by the non-zero electron beam emittance ε_y, leads to a decrease in phase velocity given by $\Delta\nu \approx 2\pi NKk\varepsilon_y/\gamma$ (see Sect. 2.2). The dispersion in the phase velocity causes the broadening of the spectral line of radiation $\Delta\lambda = \Delta\nu\lambda/2\pi N$. The typical value of $\varepsilon_y \approx \pi$ mm mrad for the emittance of the electron beam at the S-DALINAC leads to a spectral line broadening of only $\Delta\lambda \approx 0.08$ nm and thus can also not explain the observed

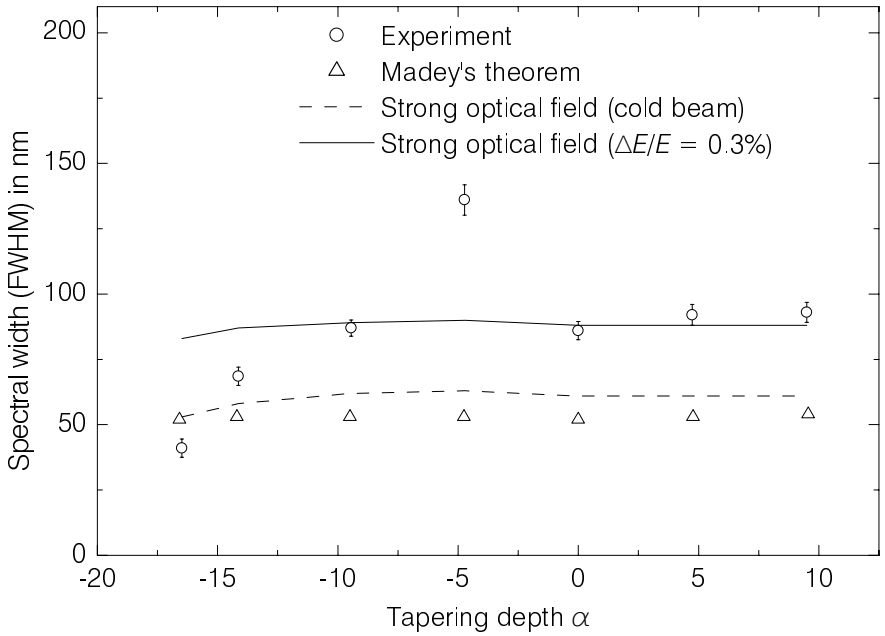

Fig. 9.7: FWHM of the spectral distribution as a function of tapering depth. Measured values (circles) are compared to those obtained using the Madey's theorem from the spectral distribution of spontaneous emission assuming a cold electron beam (triangles). The expected spectral width (FWHM) in case of strong optical field for the cold electron beam (dashed line) and for the beam having the energy spread $\Delta E_e/E_e$=0.3% (solid line) are also shown.

spectral broadening.

The influence of the electron-beam energy-spread on the gain spectrum is illustrated in Fig. 9.6. The solid line corresponds to the gain spectrum in case of a cold electron beam. The dashed line represents the gain curve of the FEL driven by an electron beam having an energy spread of $\Delta E_e/E_e = 0.3\%$ (upper limit for the electron-beam spread delivered by the S-DALINAC). Both curves were obtained using the program package of [33]. The FWHM of the gain spectrum without and with an energy spread is equal to 3.7 and 4.4, respectively.

The FWHM of the spectral distribution deduced from the width of the gain curve is shown for a cold beam (dashed line) and for a beam with energy spread (solid line) in Fig. 9.5. It shows that the increase of the spectral width by ∼150% due to the energy spread of the electron beam can indeed explain the spectral width for

the uniform undulator ($\alpha = 0$), but it can not explain the change of the spectral width for other tapering depths observed experimentally (*e.g.* $\alpha = -4.47$).

So far, the analysis has been carried out in the low current and weak optical field approximation. With the growth of the optical field strength, however, the gain spectrum changes substantially its shape (see Sect. 2.5). In the strong optical field regime the FWHM of the spectral distribution grows [23] as $\Delta\lambda \approx \lambda |u|^{1/2} / 2\pi N_u$. The spectral widths obtained taking into account the intracavity optical field strength corresponding to the parameters of this experiment are displayed in Fig. 9.7. The dashed line shows the expected line width (FWHM) for the realistic value of the intracavity field strength for the cold beam. The solid line represents the same value for the electron beam having an energy spread $\Delta E/E$=0.3%. As a reference the measured spectral widths and those obtained using Madey's theorem are represented by the same symbols as in Fig. 9.5. Again the change of the spectral width for different tapering values as observed experimentally can not be explained by the increase of the optical field strength.

Summarizing, it can be stated that the broadening of the spectral width is caused mainly by the energy spread of the electron beam.

9.3 Small signal gain change

A further important observable to study the influence of tapering is the small signal gain. It was predicted by Saldin *et al.* [20] that the maximum value of the small signal gain decreases with the tapering parameter α. To examine this prediction the values of the small signal gain obtained according to the description in Sect. 7.1 are displayed for positive and negative tapering for the Darmstadt FEL in Fig. 9.8 together with data from TJNAF [52]. The values are normalized to unity for both cases. It should be mentioned, however, that the absolute value obtained at the two different FELs differ by a factor of 100 with respect to the electron beam current. This holds also for the small signal gain which amounts to about 2% at Darmstadt and 80% at TJNAF. A comparison with the prediction (solid line) based on the analytical approach by Saldin *et al.* [20] shows a very good agreement. This is a quite remarkable finding since the theoretical approach

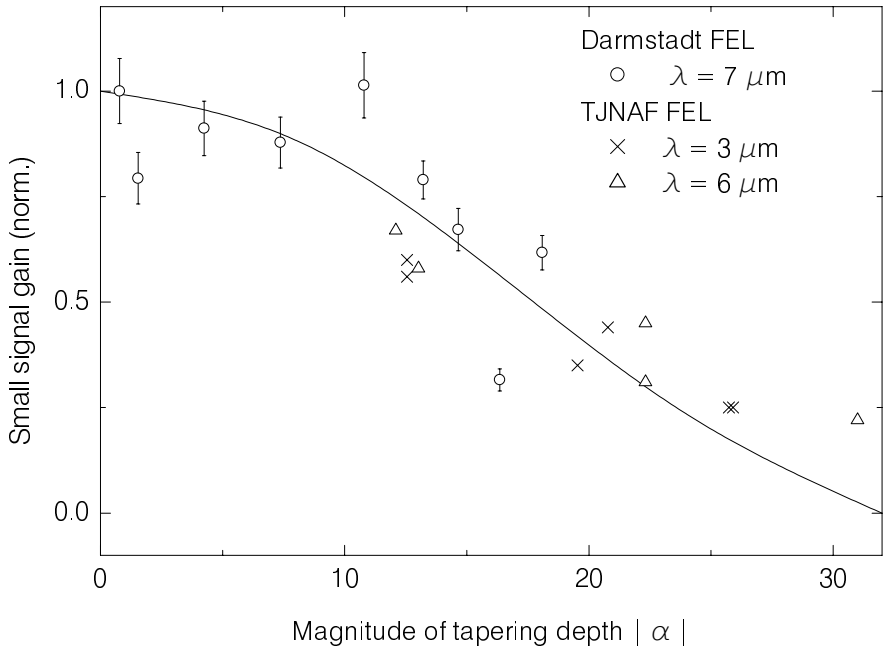

Fig. 9.8: The experimental values of the small signal gain obtained at the Darmstadt and the TJNAF FELs, respectively, at different wavelength as a function of the absolute tapering depth. The experimental values are normalized to unity. The solid line represents the theoretical predictions [20] by Saldin *et al.*

predicts correctly the dependence of the small signal gain in the low as well as in the high current regime for negative as well as positive tapering and at various wavelengths.

9.4 Efficiency change

In this section the behavior of the laser efficiency as function of the undulator tapering is studied. It is assumed that the recorded laser power is proportional to the area under the measured spectral distribution. This area has been deduced by means of a numerical integration. In order to estimate the influence of the water vapor absorption on the final result, two different methods were used. First, the measured spectra, *i.e.* neglecting a correction due to absorption by the water

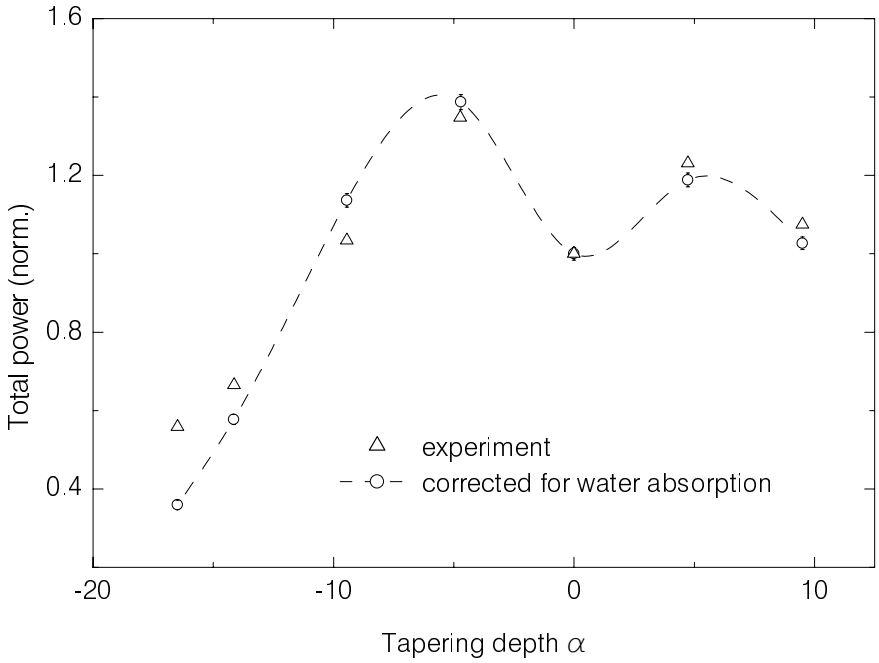

Fig. 9.9: Experimental values of the FEL power vs. tapering parameter α normalized to the value for an uniform undulator ($\alpha = 0$). The data points are obtained by integration of the spectral distribution (triangles) and are corrected for vapor absorption (circles).

vapor for those values located near the vapor absorption maxima, were integrated over the entire region using the trapezoidal rule. The values of the area under the spectrum were normalized to the value of a uniform undulator ($\alpha = 0$), Fig. 9.9 (triangles).

A second, more precise method of integration was carried out for the interval $c\pm 2d$ with a step size of 1 nm. Since the measurements were performed with a step of 5 nm and since six points were ignored because of strong water-vapor absorption, the algorithm of quadratic interpolation was used. This algorithm draws a second-order line through four neighboring points and calculates the function value for each step. The results of the numerical integration as a function of the tapering depth are presented in Fig. 9.9 as circles connected by a dashed line. The error in the determination of the area does not exceed ± 1.5 % and is within the size of the symbols.

The difference between the values as obtained by the two methods is not fundamental, since it does not change the overall picture. It becomes apparent, however

Tab. 9.1: Output peak power W measured at the Darmstadt FEL and the corresponding values of the dimensionless optical wave amplitude at saturation $u^{(\infty)}$ as well as of the reduced efficiency $\hat{\eta}$ for different values of the tapering parameter α.

α	$W \pm \Delta W$ (kW)	$u^{(\infty)} \pm \Delta u^{(\infty)}$	$\hat{\eta} \pm \Delta\hat{\eta}$
-16.48	5.2 ± 0.1	17.9 ± 0.4	1.83 ± 0.08
-14.14	8.4 ± 0.1	22.8 ± 0.5	2.96 ± 0.12
-9.44	16.5 ± 0.2	31.9 ± 0.6	5.80 ± 0.22
-4.73	20.0 ± 0.3	35.1 ± 1.2	7.02 ± 0.48
0.00	14.4 ± 0.2	30.2 ± 0.9	5.20 ± 0.30
4.74	17.2 ± 0.3	32.7 ± 1.1	6.09 ± 0.41
9.50	14.8 ± 0.2	30.3 ± 0.9	5.23 ± 0.32
14.35	8.2 ± 0.1	22.5 ± 0.5	2.89 ± 0.13

that the area under the spectrum and thus the total FEL power changes significantly for different values of the tapering depth α.

The areas of the spectral distributions were normalized to the power measured for the uniform undulator. This allows to estimate the peak power for different tapering values which is shown in the second column of Tab. 9.1. To calculate the efficiency the following procedure was used. In Sect. 2.3 the dimensionless optical wave amplitude u was defined. The value of u at saturation $u^{(\infty)}$ is determined by the vector potential of the electromagnetic laser field inside the undulator [53] and is thus proportional to the output FEL peak power W. The values of $u^{(\infty)}$ as well as the corresponding values of the normalized efficiency are calculated as described in Appendix A and are shown in Tab. 9.1, in the third and fourth columns, respectively.

In order to compare the experimental results with the predictions of the simulation, a numerical study of the saturated power has been performed. Using the parameters of the Darmstadt FEL the macropulse evolution for different values

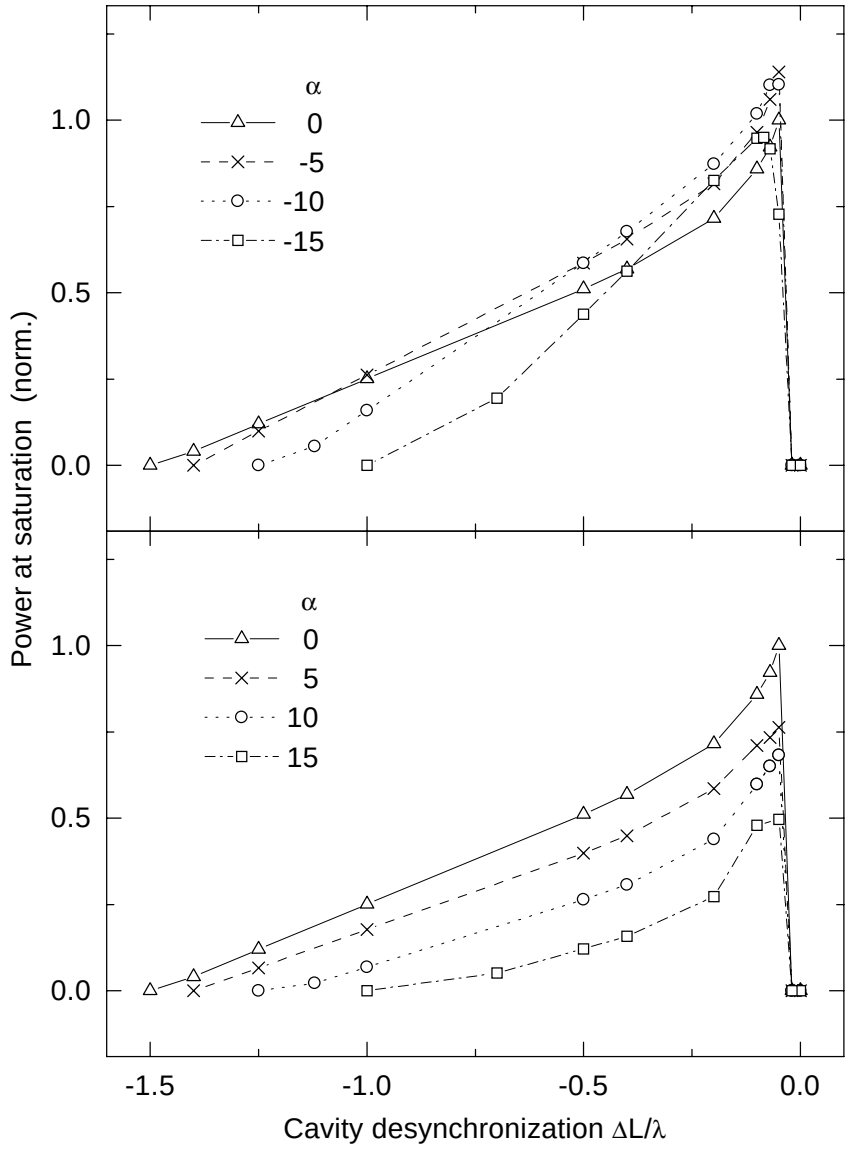

Fig. 9.10: Simulated FEL power at saturation as a function of the cavity desynchronization for different negative (top) and positive (bottom) tapering depths α, normalized by the maximum value of power for the uniform undulator. A power increase of 15% is observed for various desynchronization in case of negative tapering.

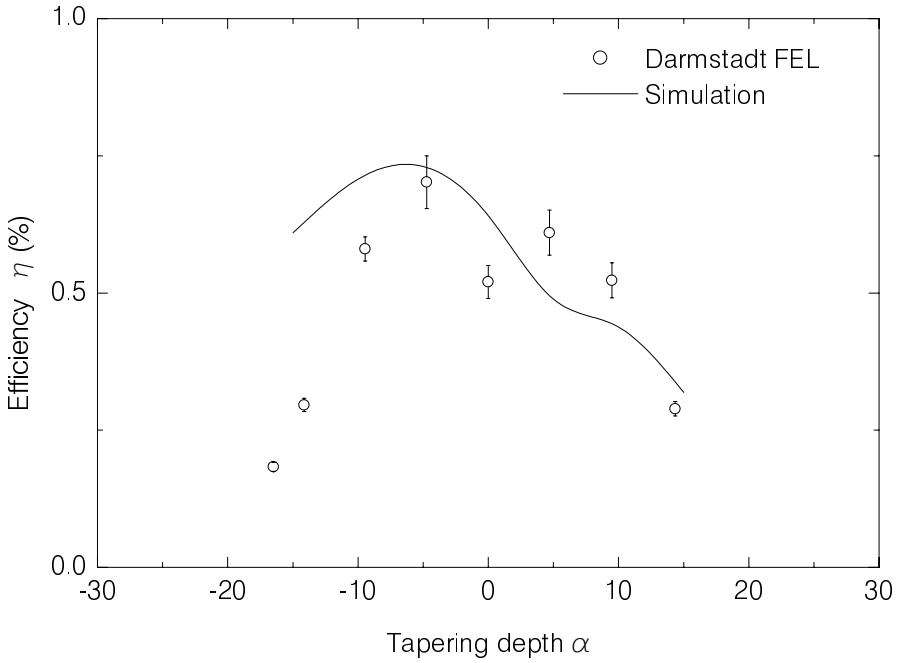

Fig. 9.11: The efficiency η of the laser light output as a function of the tapering depth α (circles) measured at the Darmstadt FEL. The solid line represents the results of the numerical simulations.

of the cavity desynchronization $\Delta L/\lambda$ and different tapering depthes α were simulated. At the steady-state regime, when the laser has reached its saturation, the power level was identified as saturated power.

Figure 9.10 shows the saturated power as a function of the cavity desynchronization for different negative and positive values of the tapering parameter α. The saturated power is normalized to the maximum value of the saturated power of the uniform undulator.

The data displayed in Fig. 9.10 show that for a positively tapered undulator (lower part) the saturation power of the FEL is always lower as compared to the case of the uniform undulator (solid line) regardless of the applied cavity desynchronization. In the case of small inverse ($\alpha < 0$) tapering (Fig. 9.10, top) for certain desynchronizations the power is predicted to reach saturation at a level that is up to about 15% higher than in the untapered case.

Figure 9.11 shows the experimental values of the efficiency $\eta = \hat{\eta}/4\pi N_u$ as a function of the tapering depth α in comparison with the results of the numerical

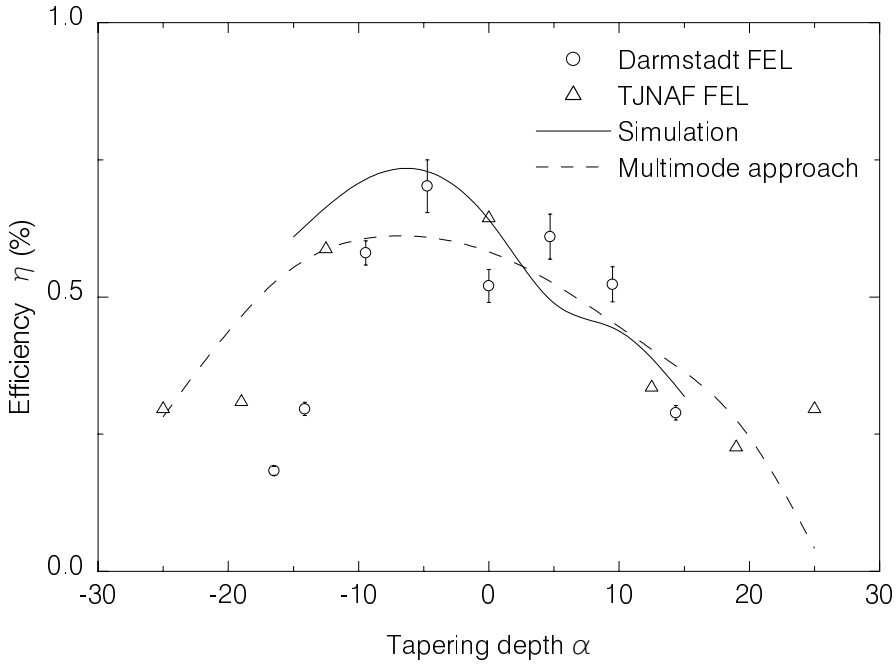

Fig. 9.12: The efficiency η of the laser output as a function of tapering depth α measured at the Darmstadt FEL (circles). The solid line represents the results of the numerical simulations (same as in Fig. 9.11). The triangles result from the measured efficiency of the TJNAF FEL [52]. The dashed line shows the results of a numerical simulation by [52] using the multimode approach.

simulation. The efficiency reaches the maximum at small values (both, positive and negative) of the tapering depth α. At $\alpha = -4.7$ the efficiency exceeds that of the uniform undulator by more than 35%. For small positive values ($\alpha = 4.7$) an increase of the efficiency of more than 18% is observed.

In Fig. 9.12 the results obtained at the Darmstadt FEL (circles) are compared with those obtained [52] at the IR DEMO FEL (triangles) at the Thomas Jefferson National Accelerator Facility (TJNAF). The results from the TJNAF are scaled by a factor of 2.2 in order to compare their behavior with the results of the Darmstadt FEL. A similar behavior of the efficiencies of both, the Darmstadt FEL and the IR DEMO FEL, is observed. The flat maximum for small values of the tapering depth α changes into a recession of the efficiency at big α values. For small negative values of α ($-10 \leq \alpha \leq 0$) the efficiency exceeds the value at the corresponding positive range of α. The dashed line represents the numerical

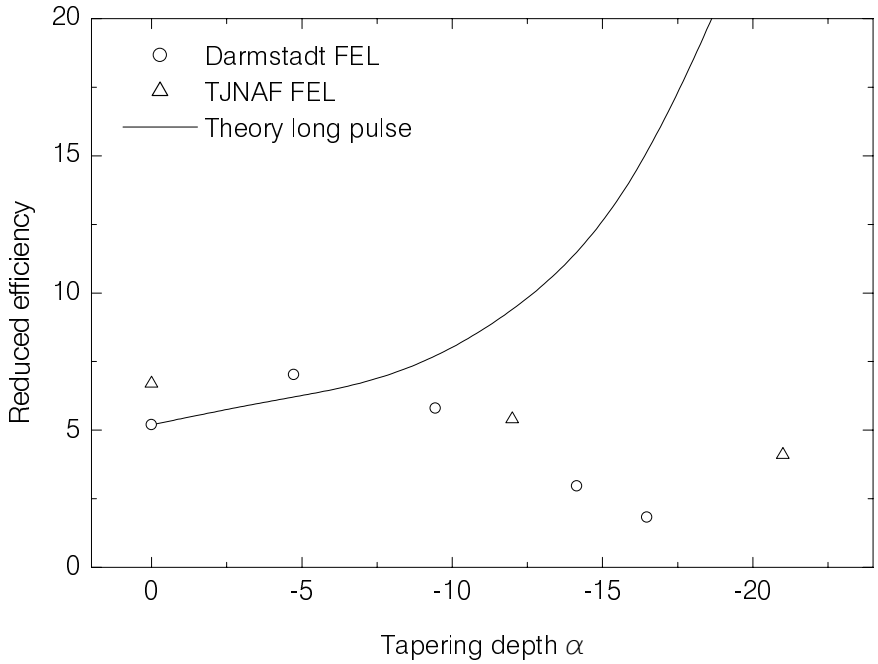

Fig. 9.13: Experimental values of the reduced efficiency $\hat{\eta} = 4\pi N_u \eta$ of the laser light output of the Darsmtadt and TJNAF FELs, respectively, as function of the tapering depth for negative values of α. The solid line is the result of a calculation by Saldin *et al.* [11] omitting short pulse effects.

results obtained in a multimode approach [52]. This calculation does not predict the possibility of an efficiency increase caused by tapering. It confirms the experimentally observed fact that efficiency decreases significantly for $|\alpha| \geq 10$. However, contrary to the simulations using the multimode theory, the simulations performed within the framework of this thesis predict an efficiency increase at small negative values of α but does not describe the experimentally observed increase of the efficiency at $0 < \alpha < 10$.

Finally it is emphasized that the observables considered in the present work can be described theoretically only by taking into account short pulse effects as discussed above. This becomes apparent by comparing the data of the Darmstadt and the TJNAF experiment with each other. In Figs. 9.13 and 9.14 the efficiency of the laser light output for both FELs is plotted as a function of a tapering depth α for both positive and negative values. The solid curve displayed in both figures results from the calculations by Saldin *et al.* [11] omitting short pulse effects. It becomes apparent that for negative tapering (Fig. 9.13) the experimental values

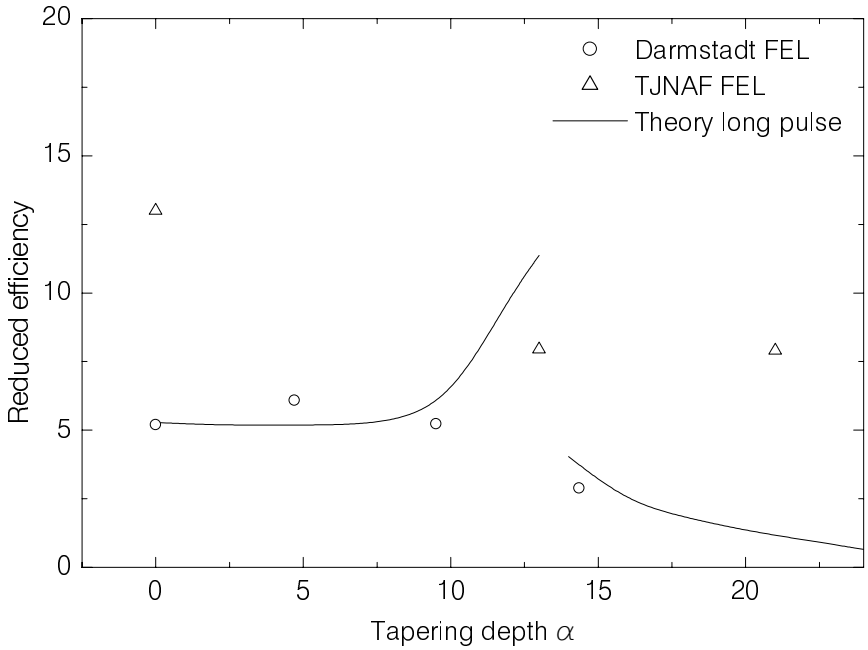

Fig. 9.14: Same as before, but for positive values of α.

are described only for small α and for a positive tapering depth only those of the Darmstadt FEL. The overall agreement with the theoretical predictions that consider long pulse effects only is not satisfactory, while the results of the numerical simulations, taking into account short pulse effects are found to be in a good agreement with the experiments.

10 Summary and outlook

Within the framework of this thesis an analysis of the experimental spectral distributions obtained [21] at the Darmstadt FEL with the tapered undulator has been performed. The experiments were carried out at an electron beam energy of 31 MeV and a wavelength of 7 μm. Experimental results for various tapering depths have been obtained with respect to the position of the maximum of the optical spectral distributions, the spectral width, the small signal gain and the efficiency of the laser light output and have been understood quantitatively. It has been found that for some values of tapering the FEL efficiency exceeds that of the uniform undulator by more than 35% and 18% for negative and positive tapering, respectively.

To investigate whether this efficiency increase has been caused by the undulator tapering, a thorough comparison of the experimental results with the predictions of a numerical simulation has been performed. For this purpose the 1D simulation code FEL1D-OSC, originally designed for the numerical study of FEL amplifiers, has been extended to the conditions of the Darmstadt FEL. The code input parameters have been adjusted and its validity has been checked by comparison with earlier results observed of the Darmstadt FEL with the uniform undulator. As a further check for the fact that the code is able to reproduce short pulse effects, test measurements at FELIX in the Netherlands have been performed. The measurements were carried out at almost the same electron bunch length and at the same wavelength as at the Darmstadt FEL, but with higher electron beam current. Under these conditionds a more prominent influence of the short pulse effects on the performance of the FEL has been expected. The observed oscillations in the macropulse power and an increase of the spectral width, caused by the FEL operation in the limit-cycle regime have indicated, indeed, the strong influence of short pulse effects and have been successfully reproduced numerically.

Furthermore, a simulation of the Darmstadt FEL, operated with the tapered undulator was performed. The same input parameters as for the uniform undulator were used. Good agreement of the numerical results with experiment has been observed with respect to the shift of the radiation wavelength, which could not be explained before by means of the long pulse model [11]. Furthermore, a qualitative comparison of the change in the small signal gain caused by tapering with

the recent results from TJNAF FEL [17] and with the long pulse model [11] has been performed. The increase of the efficiency, observed in the experiment has been compared to the results obtained numerically. Satisfactory agreement has been found for negative tapering. However, the results of the numerical simulations were not able to explain the observed increase of the efficiency of the laser light output caused by positive tapering. The possible reason for this could be 3D effects which were not taken into account by the simulation code. However, the use of a 3D time-dependent code is at the moment a problem which can not be solved with the existing computers within a reasonable time for a typical macropulse length of the Darmstadt FEL. The change in the efficiency observed at the Darmstadt FEL has also been compared to recent results from TJNAF and to numerical predictions made within the framework of the multimode model performed in [52]. Good agreement in the range of a large absolute values of α ($|\alpha| \geq 10$) between both experimental as well as both numerical results has been observed. Furthermore, the enhancement of the efficiency of the laser light output observed at the Darmstadt FEL could only be explained by the simulations performed within the framework of this thesis and only for the case of negative tapering.

It becomes evident that tapering of the undulator leads to completely different results in the case of FEL amplifiers compared to the FEL oscillators. As mentioned above in case of an FEL amplifier an substantial efficiency increase has been observed. As predicted theoretically [11] and as shown in the present work the effects amount only to about 20% for an FEL oscillator which is rather moderate only and is insufficient for practical purposes.

For further efficiency enhancement of the laser light output a modification is proposed which includes an additional segment – the so-called pre-buncher – to the existing undulator. For this arrangement a further efficiency enhancement is expected [25]. The numerical code used within the framework of this thesis is able to estimate this effect.

A Calculation of the FEL efficiency

The reduced efficiency in Sect. 9.4 has been calculated using Eq. (3.19) from [25] which has the form $\hat{\eta} = \hat{\sigma}(u^{(\infty)})^2/2$, where $\hat{\sigma}$ is the reduced parameter of the resonator losses and $u^{(\infty)}$ is the dimensionless optical wave amplitude at saturation.

In Sect. 2.3 the dimensionless optical wave amplitude u has been defined. Its value u at saturation $u^{(\infty)}$ is determined by the vector potential of the electromagnetic laser field inside the undulator A as $u^{(\infty)} = 4.242 \cdot 10^{-5} A$ [53]. The intracavity laser power density P of a linearly polarized light is related [53] to the vector potential A by $P_0 = 21.5(Ar_w/\lambda)^2$, where r_w is the optical beam waist radius. Thus, for the Darmstadt FEL operating at 7 μm and having the optical beam profile as shown in Fig. 6.1 the value A is equal to $A = 4.57 \cdot 10^{-4}\sqrt{P_0[GW/cm^2]}$. If, *e.g.* for the resonator with the mirror having the reflectivity of 99.8%, the peak power of 100 kW is extracted, the average intracavity power density is $P_{av} = 0.146$ GW/cm^2. Since the optical beam waist radius exceeds the average electron beam radius, not the average power density but its maximum value in the center $P = (2/\sqrt{\pi})P_{av}$ should be taken into account. Then $A = 1.85 \cdot 10^{-4}$ and $u^{(\infty)} = 78.5$

The reduced parameter of resonator losses $\hat{\sigma} = \sigma/j$, where losses $\sigma = 0.009$ include absorption and reflection from the mirrors and diffraction losses inside the resonator [36]. The dimensionless beam current j is defined according Eq. (21) from [23] as $j = 4.69 \cdot 10^{-10} n_e$, where n_e is the electron density. The filling factor $F = (r_b/r_\omega)^2$, where r_b and r_ω are electron beam and optical waist radii, respectively, is included into the dimensionless beam current j. For the peak beam current of 2.7 A and the micropulse length of 2 ps the dimensionless current is j =0.79 and $\hat{\sigma}$=0.0114.

References

[1] J.M.J. Madey, *Stimulated emission of bremsstrahlung in a periodic magnetic field*, Journ. Appl. Phys. **42** (1971) 1906.

[2] D.A.G. Deacon, L.R. Elias, J.M.J. Madey, G.J. Ramian, H.A. Schwettman, T.I. Smith, *First operation of a free-electron laser*, Phys. Rev. Lett. **38** (1977) 892.

[3] J.A. Edighoffer, G.R. Neil, C.E. Hess, T.I. Smith, S.W. Fornaca, H.A. Schwettman, *Variable-wiggler free-electron laser oscillator*, Phys. Rev. Lett. **52** (1984) 344.

[4] R.W. Warren *et al.*, *First operation of the Los Alamos free-electron laser*, Proc. of the International Conference on lasers '83, Ed. R. C. Powell, STS Press, McLean, VA, (1983).

[5] M. Billardon *et al.*, *First operation of a storage ring free-electron laser*, in Free electron generators of coherent radiation, ed. C. A. Brau, *et al.*, SPIE, Bellingham, WA (1984).

[6] A. Richter, *Operational experience at the S-DALINAC*, Proc. of the Fifth EPAC, Eds. S. Meyers, A. Pacheco, R. Pascual, C. Petit-Jean-Genaz, J. Poole, IOP Publishing, Bristol (1996) 110.

[7] A. Richter, *Der neue Freie-Elektronen-Laser in Darmstadt*, Physikalische Blätter **54** (1998) 31.

[8] N. Kroll, P. Morton, M. Rosenbluth, IEEE Journ. Quant. Electr. **38** (1980) 891.

[9] T.J. Orzechovski, B.R. Anderson, J.C. Clark, W.M. Fawley, A.C. Paul, D. Prosnitz, E.T. Scharlemann, S.W. Yarema, D.B. Hopkins, A.M. Sessler, J.S. Wurtele, *High-efficiency extraction of microwave radiation from a tapered-wiggler free-electron laser*, Phys. Rev. Lett. **57** (1986) 2172.

[10] H.P. Freund, T.M. Antonsen, *Principles of Free-electron Lasers*, 2^{nd} edition, Chapman & Hall, London, (1996).

[11] E.L. Saldin, E.A. Schneidmiller, M.V. Yurkov, *The features of an FEL oscillator with a tapered undulator*, Optics Communications **103** (1993) 297.

[12] E.L. Saldin, E.A. Schneidmiller, M.V. Yurkov, *Some novel features of an FEL oscillator with tapered undulator*, Nucl. Instr. Meth. A **375** (1996) 336.

[13] R. Prazeres, J.M. Berset, F. Glotin, D. Jaroszynski, J.M. Ortega, *Optical perfomance of the CLIO infrared FEL*, Nucl. Instr. Meth. A **331** (1992) 15.

[14] P.W. van Amersfoort, R.J. Bakker, J.B. Bekkers, R.W.B. Best, R. van Buuren, P.F.M. Delmee, B. Faatz, C.A.J. van der Geer, D.A. Jaroszynski, P. Manintveld, W.J. Mastop, B.J.H. Meddens, A.F.G. van der Meer, J.P. Nijman, D. Oepts, J. Pluygers, M.J. van der Wiel, W.A. Gillespie, P.F. Martin, M.F. Kimmitt, C.R. Pidgeon, M.W. Poole, G. Saxon, *First lasing with FELIX*, Nucl. Instr. Meth. A **318** (1992) 42.

[15] D.A. Jaroszynski, R. Prazeres, F. Glotin, J.M. Ortega, D. Oepts, A.F.G. van der Meer, G.M.H. Knippels, P.W. van Amersfoort, *Free-electron laser efficiency enhancement, gain enhancement, and spectral control using a step-tapered undulator*, Phys. Rev. Lett. **74** (1995) 2224.

[16] D.A. Jaroszynski, R. Prazeres, F. Glotin, J.M. Ortega, D. Oepts, A.F.G. van der Meer, G. Knippels, P.W. van Amersfoort, *Free-electron laser operation and self-amplified spontaneous emission using a step-tapered undulator*, Nucl. Instr. Meth. A **358** (1995) 228.

[17] A. Christodoulou, D. Lampris, W.B. Colson, P.P. Crooker, J. Blau, R.D. McGinnis, S.V. Benson, J.F. Gubeli, G.R. Neil *Simulations of the TJNAF FEL with tapered and inversed tapered undulators*, Nucl. Instr. Meth. A **475** (2001) 182.

[18] J. Blau, V. Bouras, W.B. Colson, K. Polikandriotis, A. Kalfoutzos, S.V. Benson, G.R. Neil, *Simulations of the 100 kW TJNAF FEL using the step-tapered undulator*, Nucl. Instr. Meth. A **483** (2002) 138.

[19] S. Benson, J. Gubeli, G.R. Neil, *An experimental study of an FEL oscillator with a linear taper*, Nucl. Instr. Meth. A **475** (2001) 276.

[20] E.L. Saldin, E.A. Schneidmiller, M.V. Yurkov, *High efficiency FEL oscillator with time dependent undulator tapering*, Phys. Rev. Lett. A **185** (1994) 469.

[21] T. Wesp, *Messung und Optimierung optischer Parameter des Darmstädter Freie-Elektronen-Laser und Vermessung und Justierung der Strahlführungselemente des S-DALINAC*, Dissertation, Technische Universität Darmstadt (1998), D17.

[22] E.L. Saldin, E.A. Schneidmiller, M.V. Yurkov, *Statistical properties of radiation from VUV and X-ray free electron laser*, Optics Communications **148** (1998) 383.

[23] W.B. Colson, *Classical free electron laser theory*, in Laser Handbook, vol. 6, Eds. W. B. Colson, C. Pellegrini, A. Renieri, Elsevier Science Publishers B.V. (1990).

[24] R. Walker, *Insertion devices: undulators and wigglers* CERN Accelerator School on Synchrotron radiation and Free Electron Lasers, CERN 98-04

[25] E.L. Saldin, E.A. Schneidmiller, M.V. Yurkov, *The Physics of Free Electron Lasers*, Springer-Verlag, Berlin (2000).

[26] C.A. Brau, *Free-Electron Lasers*, Academic Press, Inc., Boston, (1990).

[27] W.B. Colson and S.K. Ride, *The Free Electron Laser: Maxwell's Equations Driven by Single-Particle Currents*, in Physics of Quantum Electronics, vol. 7, Addison-Wisley, Reading, MA (1980).

[28] R.W. Warren, J.S. Goldstein, B.E. Newnam, *Spiking mode operation for a uniform-period wiggler*, Nucl. Instr. Meth. A **250** (1986) 19.

[29] S.J. Hahn and J.K. Lee, *Nonlinear short-pulse propagation in a free-electron laser*, Phys. Rev. E **48** (1993) 2162.

[30] S.J. Hahn and J.K. Lee, *Bifurcations in a short-pulse free-electron laser oscillator*, Phys. Lett. A **176** (1993) 339.

[31] N. Kroll, P. Morton, M. Rosenbluth, IEEE Journ. Quant. Electr. **17** (1981) 1436.

[32] N.M. Kroll, P.L. Morton, M.N. Rosenbluth, *Variable parameter free-electron laser*, in Physics of Quantum Electronics, vol. 7, Addison-Wesley, Reading, MA (1980).

[33] A.Yu. Mosolov, E.L. Saldin, E.A. Schneidmiller, M.V. Yurkov, *Program Package for 1D Simulations of Free Electron Lasers*, Dubna, (1995).

[34] W.B. Colson, R.D. McGinnis, *The free electron laser with inverse taper*, Nucl. Instr. Meth. A **445** (2000) 49.

[35] R.J. Bakker, D.A. Jaroszynski, A.F.G. van der Meer, D. Oepts and P.W. van Amersfoort, *Short-pulse effects in a free-electron laser*, IEEE Journ. Quant. Electr. **30** (1994) 1635.

[36] M. Brunken, S. Döbert, R. Eichhorn, H. Genz, H.-D. Gräf, H. Loos, A. Richter, B. Schweizer, A. Stascheck, T. Wesp, *First lasing of the Darmstadt cw free electron laser*, Nucl. Instr. Meth. A **429** (1999) 21.

[37] M. Brunken, S. Döbert, H. Genz, M. Gopych, H.-D. Gräf, S. Khodyachykh, S. Kostial, U. Laier, H. Loos, A. Richter, S. Richter, B. Schweizer, A. Stascheck, O. Titze, *Operation of the S–DALINAC, Related Topics and Developments*, Proc. of the 9$^{\text{th}}$ Workshop on RF Superconductivity, Los Alamos Report LA-13782-C (2000) 65.

[38] P. Mohr, J. Enders, T. Hartmann, H. Kaiser, D. Schiesser, S. Schmitt, S. Volz, F. Wissel, A. Zilges, *Real photon scattering up to 10 MeV: The improved facility at the Darmstadt electron accelerator S–DALINAC*, Nucl. Instr. Meth. A **423** (1999) 480.

[39] T. Hartmann, J. Enders, P. Mohr, K. Vogt, S. Volz, A. Zilges, *Measurement of the dipole and electric quadrupole strength distribution up to 10 MeV in the doubly magic nuclei ^{40}Ca and ^{48}Ca*, Phys. Rev. Lett. **85** (2000) 274.

[40] P. Mohr, C. Vogt, M. Babilon, J. Enders, T. Hartmann, C. Hutter, T. Rauscher, S. Volz, A. Zilges, *Experimental simulation of a stellar photon bath by bremsstrahlung: The astrophysical γ-process*, Phys. Lett. B **488** (2000) 127.

[41] J. Freudenberger, H. Genz, V.V. Morokhovskii, V.L. Morokhovskii, U. Nething, A. Richter, R. Zahn, J.P.F. Sellschop, *Lineshape, linewidth and spectral density of parametric x-radiation at low electron energy in diamond*, Appl. Phys. Lett. **70** (1997) 267.

[42] V.V. Morokhovskii, K.H. Schmidt, G. Buschhorn, J. Freudenberger, H. Genz, R. Kotthaus, A. Richter, M. Rzepka, P. Weinmann, *Polarization of Parametric X Radiation*, Phys. Rev. Lett. **79** (1997) 4389.

[43] H. Genz, K. Gerstner, H.-D. Gräf, R. Hahn, H. Jennewein, A. Richter, B. Schweizer, T. Tschudi, *Absolute measurement of the resonator length of the Free Electron Laser at the S-DALINAC with a modulated semiconductor laser,* to be published in Nucl. Instr. Meth. A.

[44] H. Weise, *Entwicklung, Aufbau und Betrieb eines Hochstrominjektors mit subharmonischem Chopper- und Prebunchersystem für den Freie-Elektronen-Laser am S–DALINAC*, Dissertation, Technische Hochschule Darmstadt (1992), D17.

[45] M. Brunken, *Entwicklung eines Autokorrelators zur Messung der Mikropulsdauer and Aufbau eines Er:YAG-Lasers zur Verstärkung der Mikropulse am Freie-Elektronen-Laser*, Dissertation, Technische Universität Darmstadt, (2002), D17.

[46] Spectra Technology, Inc., private communication.

[47] B. Faatz, *Transverse mode analysis of hole-coupled free-electron lasers*, Dissertation, Utrecht (1992).

[48] E.L. Saldin, E.A. Schneidmiller, M.V. Yurkov, private communication.

[49] K. Alrutz-Ziemssen, *Auslegung und Konstruktion eines Freie-Elektronen-Lasers im nahen Infraroten am supraleitenden Darmstädter Elektronenbeschleuniger*, Dissertation, Technische Hochschule Darmstadt (1990), D17.

[50] H. Loos, *Bestimmung der longitudinalen Struktur der Elektronenbunche im Strahl von supraleitenden Beschleunigern*, Dissertation, Technische Universität Darmstadt (2001), D17.

[51] International Union of Pure and Applied Chemistry, *Tables of wavenumbers for the calibration of IR Spectrometers*, Butterworths, London (1961).

[52] A. Christodoulou, D. Lampiris, K. Polykandriotis, W.B. Colson, P.P. Crooker, S. Benson, J. Gubeli, G.R. Neil, *Free-Electron-Laser oscillator with a linear taper*, Phys. Rev. E **66** (2002) 056502.

[53] P. Sprangle, A. Ting, E. Esarey, A. Fisher, *Tunable, short pulse hard x-ray from a compact laser synchrotron source*, J. Appl. Phys. **72 (11)** (1992) 5032.

Danksagung

An dieser Stelle möchte ich all denen Personen meinen Dank aussprechen, die mich bei der Entstehung dieser Arbeit unterstützt haben.

Herrn Professor Dr. Dr. h.c. mult. Achim Richter danke ich nicht nur dafür, daß er mich in seiner Arbeitsgruppe aufnahm und mir damit die Möglichkeit gab, an der Technischen Universität Darmstadt zu promovieren, sondern auch für sein stetes Interesse am Fortgang dieser Arbeit. Außerdem danke ich auch dafür, daß er mir die Teilnahme an mehreren FEL Konferenzen, Messungen am FELIX und meine Reisen nach DESY ermöglicht hat.

Herrn Professor Dr.-Ing. Wolfgang Seelig danke ich für die Übernahme des Korreferats.

Mein besonderer Dank gilt Herrn Dr. Harald Genz für die ständige Unterstützung, zahlreiche Diskussionen und wichtige Hinweise. Außerdem bin ich sehr dankbar für das sorgfältige Durchlesen dieser Arbeit.

Bei Herrn Dr. Otto Titze and Frau Dr. Simone Richter möchte ich mich für die ständige Unterstützung in Computerfragen bedanken. Herrn Dr. Hans-Dieter Gräf danke ich für die Diskussionen, die dieser Arbeit sehr geholfen haben.

I would like to thank Dr. Evgeny Saldin, Dr. Evgeny Schneidmiller and Dr. Mikhail Yurkov for the numerous useful discussions, their permanent interest in the progress of this work and for the extension of their simulation code to the conditions of the Darmstadt FEL.

I am also grateful to Dr. Vivek Asgekar for fruitful discussions and valuable advices.

Bei meinen Kollegen aus der FEL-Gruppe, Herrn Dr. Thorsten Wesp, Herrn Dr. Henrik Loos, Herrn Dr. Bernd Schweizer, Herrn Dr. Marco Brunken, Herrn Dipl.-Phys. Christoph Heßler und Herrn. Dipl.-Phys. Lars Casper möchte ich mich vielmals für die tatkräftige Unterstützung bedanken.

Den Herren Artem Shevchenko, Aleksey Burda, Maksim Miski-Oglu und Anton Karnaukhov möchte ich meinen Dank aussprechen für ihren Einsatz bei der Erstellung dieser Arbeit.

Last, but not least, I would like to thank my parents, Dr. Aleksey Khodyachykh and Alla Khodyachykh for their support. Even despite the large distance between Kharkiv and Darmstadt, their thoughts and their care were permanently helping me.

Diese Arbeit wurde gefördert durch Mittel aus dem Graduiertenkolleg "Physik und Technik von Beschleunigern" der DFG unter der Nummer 410/2-01 und der DFG Forschergruppe FOR 272/2-1 "Untersuchung von Vielteilcheneffekten in Atomkernen mit Elektronen und Photonen am S-DALINAC und die damit verbundene Weiterentwicklung des Beschleunigers".

Lebenslauf

Sergiy Khodyachykh

26. Dezember 1975	Geboren in Kharkiv, Ukraine
1982 – 1992	Besuch der Sekundärschule Nr. 62, Kharkiv, Ukraine
1992 – 1998	Studium der Physik an der Fakultät für Physik und Technik der Kharkiver Staatsuniversität (jetzt *Karazin Kharkiv National University*), Ukraine. Vertiefungsrichtung - Kernphysik
1995 – 1996	Ausbildung zum Offizier
1997 – 1998	Diplompraktika, *National Scientific Center "KIPT"* Kharkiv, Ukraine
Februar 1998	Abschluss des Studiums mit Diplom
1998	Wissenschaftlicher Mitarbeiter, *National Scientific Center "KIPT"* Kharkiv, Ukraine
1998 – 2001	Stipendiat des Graduiertenkollegs "Physik und Technik von Beschleunigern" an der Technische Universität Darmstadt
seit Dezember 2001	Wissenschaftlicher Mitarbeiter am Institut für Kernphysik der Technische Universität Darmstadt

Erklärung:

Hiermit erkläre ich, dass ich die vorliegende Dissertation selbständig verfasst, keine anderen als die angegebenen Hilfsmittel verwendet und bisher noch keinen Promotionsversuch unternommen habe.

Darmstadt, im Oktober 2002